

Master Thesis

Influence of microstructure on fatigue properties of Nickel-based superalloys

Naomi Piera Bellomo

Supervisor PoliTo

Prof. Dr.-Ing. Sara Biamino

Supervisor KIT

Prof. Dr.-Ing. Martin Heilmaier

Supervisors MTU

Ing. Markus Fried

Ing. Frank Voese

Final Report for the Thesis
Master in Materials Engineering



Department of Applied Science and Technology
Polytechnic University of Turin
Italy, Turin
December 2019

Einfluss der Mikrostruktur auf die Ermüdungseigenschaften von Nickelbasis Superlegierungen

Masterarbeit
von

cand. M.Sc.

Naomi Piera Bellomo

Matr. -Nr. 2236631

Betreuer PoliTo

Prof. Dr.-Ing. Sara Biamino

Betreuer KIT

Prof. Dr.-Ing. Martin Heilmaier

Betreuer MTU

Ing. Markus Fried

Ing. Frank Voese

Dezember 2019

Sperrvermerk

Diese Abschlussarbeit enthält vertrauliche Informationen und Daten der MTU Aero Engines AG, die der Geheimhaltung unterliegen. Diese Abschlussarbeit darf Dritten, mit Ausnahme der betreuenden Dozenten und den Mitgliedern des Prüfungsausschusses, ohne ausdrückliche Zustimmung der MTU Aero Engines AG nicht zugänglich gemacht werden. Veröffentlichungen oder Vervielfältigungen der betreuenden – auch nur auszugsweise – sind nicht gestattet.

Dieser Sperrvermerk gilt für drei Jahre nach Übergabe der Abschlussarbeit an die Hochschule.



Influence of microstructure on fatigue properties of Nickel-based superalloys

Life prediction of directionally solidified components

Autor

Naomi Piera Bellomo

Academic Supervisors

Prof. Sara Biamino

Prof. Martin Heilmaier

Company Supervisors

Ing. Markus Fried

Ing. Frank Voese

Abstract

Bicrystal specimens have been analyzed for a fatigue life prediction using a finite element model. The aim was to understand the role of misorientation and grain boundary inclination on the material fatigue resistance. The results obtained from the simulations have been compared with experiments. The samples, bicrystals made of Nickel-based superalloy MAR M 247, were tested under LCF conditions. A good agreement between the model and the experiments has been observed. SEM investigations of the tested specimens revealed that the failure points are located near the grain boundary, in accordance with FEM predictions. By inspecting the fracture surfaces it is possible to assume that, the reason for failure is mostly due to pores, at lower temperatures, and oxidation, at higher temperatures. These results are comparable to the single crystal ones.

Acknowledgment

First, I would like to thank the thesis supervisors in the company, Ing. Markus Fried and Ing. Frank Voese. Ing. Fried has always been there for me when I needed it. As a perfect mentor, he followed my path within the company and the development of my work with attention and interest, offering his support with patient and commitment. I am equally grateful to Ing. Voese, who guided me through the concepts of finite element modelling with constancy and enthusiasm. I also thank my academic supervisors, Prof. Martin Heilmaier, professor at Karlsruhe Institute of Technology, and Prof. Sara Biamino, professor at the Polytechnic of Turin. Both have made a significant contribution to my work with suggestions and technical advice based on years of experience.

I would like to express my gratitude to all the members of TEWT team at MTU and especially to Dr. Thomas Goehler, Ing. Michael Weiss and Dr. Caspar Schwalbe for making me feel part of this beautiful group.

With great affection I thank my friends, those left in Italy and those who made me feel at home also in Germany: Michele Milia, Nicola Ghiani, Luca Merante, Alessio Vergari, Alessandro Micero, Lena Krukova, Francesca Cacciagrano, Fernando Ramirez and many others who, even if not mentioned here, have all my gratitude. A special thanks goes to Emanuele Mottola, who also in this circumstance taught me to tackle obstacles with more lightness, transforming the highest mountains into small hills.

I thank my family immensely for having believed in me and always been by my side. More than any other I want to thank my mother: she has been close to me in moments of joy and above all in those difficulty, teaching me what it means to persevere and strive to achieve goals. The great satisfaction I feel at this moment is also due to her support, her precious advice and her love.

Le cose belle sono difficili.

Contents

1	Introduction	17
1.1	State of the art	17
1.2	Objective of the master thesis	21
2	Material	23
2.1	General Properties	23
2.2	Composition and Microstructure	24
2.3	Casting defects	29
3	Fatigue	31
4	Experiments	33
4.1	The specimen	33
4.2	Testing conditions	36
4.3	Results	38
4.3.1	Strain	38
4.3.2	Stress	39
4.4	Characterization	40
4.4.1	SEM	40
4.4.2	EBSD	47
5	Simulations	50
5.1	Introduction	50
5.2	The 3D model	50
5.3	The script	52
5.3.1	Orthotropic and cubic linear elasticity model	53
5.3.2	Crystal plasticity model	54
5.3.3	Conditions of simulations	55
6	Discussion	58
6.1	Grain boundary and primary misorientation	58
6.1.1	Elastic model	58
6.1.2	Plastic model	63
6.2	Secondary misorientation	66
6.3	Comparison between experiments and simulations	68
6.4	Life prediction	69
7	Conclusion	71

A Appendix	73
A.1 The weakest-link theory	73

List of Figures

1.1	(a) Schematic drawing of an ideal directionally solidified microstructure [3], (b) Micrograph of an etched directionally solidified blade and a magnifications with the sketch of its columnar grains [4].	18
1.2	Micrograph and EBSD analysis of a Freckle chain on vane made of MAR M 247. The EBSD analysis make possible to observe the main crystallographic orientation of the mentioned component (in red) and the equiaxed grains of the Freckle chain with different crystallographic orientations (and consequently colors different from red) [2].	18
1.3	Foreign grain marked on a component, made of MAR M 247, visualized after etching. The Foreign grain is spontaneously nucleated on the surface of the component during solidification. The different crystallographic orientation is clearly visible due to the different colors between the grain marked with the withe circle and the remaining part of the component [2].	19
1.4	Inclined grain boundary on a component made of MAR M 247, visualized after etching. The different crystallographic orientation is clearly visible due to the different colors between the grain marked with the yellow circle and the remaining part of the component [2].	19
1.5	Micrograph and EBSD analysis of a transverse grain boundary (TGB). The different crystallographic orientation is clearly visible due to the different colors of the grains in the EBSD analysis. [2].	20
2.1	Examples of blades with different grain structures: (a) Polycrystalline, (b) Columnar grains, (c) Single crystal [13].	24
2.2	Important elements in the constitution of nickel-based alloys [14].	24
2.3	EBSD-coloring according to inverse pole figure in X-direction [2]. The reference coordinate system is reported here.	26
2.4	EBSD-coloring according to inverse pole figure in Y-direction [2]. The reference coordinate system is reported here.	26
2.5	EBSD-coloring according to inverse pole figure in Z-direction [2]. The reference coordinate system is reported here.	27
2.6	Color scaling representing the grains orientations' distribution [2].	27
2.7	γ/γ' in dendritic core within a grain [2].	27
2.8	BSE analysis of carbides at the grain boundary [2].	28
2.9	SE analysis of carbide at the grain boundary [2]. Carbides circled by red marks.	28
2.10	Correlation between predicted defect size and obtained life-time [8].	29

3.1	Example of a fracture surface of a fatigue failure showing the striations [21]. The crack propagates from the crack initiation point until the final overloaded fracture surface.	31
3.2	Example of a Wöhler curve, adapted from [23]. The value of N_f can be used to distinguish between low and high cycle fatigue, respectively represented by two different slopes for the curve.	32
4.1	Sketch of the bicrystal plate used to obtain the specimens [2]. The solidification direction ($\langle 001 \rangle$) is the same for the two grains. Their misorientation is represented by the values of φ that can be 16° , 32° or 45° . The loading direction is coincident with the orientation of <i>Grain 1</i> : $\langle 010 \rangle$	34
4.2	Blanks after etching [2]. The red lines represent the grain boundary between the two grains.	34
4.3	Adapted technical draw of tested LCF specimen [2]. Dimensions given in millimeters.	35
4.4	Final shape of the LFC specimen [2].	35
4.5	Sketches of samples having $\alpha = 0^\circ$ (a), and $\alpha = 45^\circ$ (b). The misorientation φ can have each of the indicated values; adapted picture from [2].	37
4.6	Normalized strain range against number of cycles to failure for specimens tested at 600°C	38
4.7	Normalized strain range against number of cycles to failure for specimens tested at 980°C	39
4.8	Normalized nominal stress range against the number of cycles to failure (600°C).	39
4.9	Normalized nominal stress range against the number of cycles to failure (980°C).	40
4.10	SEM characterization of the single crystal <i>Sample 2_SC_600</i> , (600°C); adapted picture from [2].	41
4.11	SEM characterization of the single crystal <i>Sample 1_SC_980</i> , (980°C); adapted picture from [2].	42
4.12	SEM characterization of the bicrystal <i>Sample 5_BC_600</i> , (600°C), adapted [2].	43
4.13	SEM characterization of the bicrystal <i>Sample 7_BC_600</i> , (600°C), adapted [2].	44
4.14	SEM characterization of the bicrystal <i>Sample 10_BC_600</i> , (600°C) [2].	44
4.15	SEM characterization of the bicrystal <i>Sample 5_BC_980</i> , (980°C); adapted picture from [2].	45
4.16	Comparison between two oxidized surface at 600°C (left) and 980°C (right); adapted picture from [2].	46
4.17	SEM characterization of the bicrystal <i>Sample 9_BC_980</i> , (980°C) [2].	46
4.18	Sketch of sample and the reference cutting plane for EBSD measurements [2].	47
4.19	Reference system for the sample located inside the microscope.	48
4.20	EBSD characterization for <i>Sample 1-7</i> , pictures (a)-(g) [2].	49
5.1	CAD geometry of the LCF specimen drawn with Hypermesh.	51
5.2	CAD geometry of the LCF specimen with the generated mesh.	51

5.3	CAD geometry with the two different sets of elements.	52
5.4	Normalized peak stress as a function of the element size.	56
5.5	Normalized stress range as a function of the number of cycles at 600°C, strain controlled mode; adapted graph from [2].	56
5.6	Normalized stress range as a function of the number of cycles at 980°C, strain controlled mode; adapted graph from [2].	57
6.1	Stress concentration factor against grain boundary inclination (α) for <i>Series 1</i> (a), <i>Series 2</i> (b), and <i>Series 3</i> (c).	60
6.2	Stress concentration factor against grain boundary inclination (α) for <i>Series 1</i> (a), <i>Series 2</i> (b), and <i>Series 3</i> (c).	61
6.3	Stress distribution as a function of α , for $\varphi = 16^\circ$ (a), $\varphi = 32^\circ$ (b), and $\varphi = 45^\circ$ (c).	62
6.4	Stress concentration factor as a function of α at 600°C, for $\varphi = 16^\circ$ (a), $\varphi = 32^\circ$ (b), and $\varphi = 45^\circ$ (c).	64
6.5	Stress concentration factor as a function of α at 980°C, for $\varphi = 16^\circ$ (a), $\varphi = 32^\circ$ (b), and $\varphi = 45^\circ$ (c).	65
6.6	Sensibility study for secondary misorientation at 600°C (a), 980°C (b).	67
6.7	Comparison between experiments and simulations for 600°C.	68
6.8	Life prediction: comparison between experiments and plastic simulations (logarithmic scale).	69
6.9	Life prediction: comparison between experiments and plastic simulations with Euler angles (logarithmic scale).	70
6.10	Life prediction: comparison between the conventional script (basic script) and the one with the Euler angles (logarithmic scale).	70

List of Tables

2.1	M 247 composition [17].	25
2.2	The Euler angles.	26
2.3	The γ' fraction [2].	28
4.1	Bicrystal specimens, 600°C.	36
4.2	Bicrystal specimens, 980°C.	36
4.3	Single crystal specimens, 600°C.	37
4.4	Single crystal specimens, 980°C.	37
4.5	Cause of failure of bicrystal specimens tested at 600°C.	42
4.6	Cause of failure of bicrystal specimens tested at 980°C.	43
4.7	Bicrystal specimens, EBSD analysis.	47
4.8	Euler angles determined with EBSD characterization.	48
4.9	Values of α and φ : EBSD VS Assumption.	48
5.1	Element size sensitivity study: testing conditions.	55
5.2	Element size values.	55
6.1	List of the elastic simulations and their configuration.	59
6.2	List of the elastic simulations executed and their configuration.	66
6.3	Sensibility study for the secondary misorientation at 600°C.	66
6.4	Sensibility study for the secondary misorientation at 980°C.	66
6.5	Maximum and minimum values of f_σ and f_l	68

Chapter 1

Introduction

1.1 State of the art

It is well known that materials, and consequently the components made out of them, are not perfect. In fact, they may have defects, potentially coming from each of the production steps. These defects affect properties of the material, that is usually considered to be homogeneous. The presence of irregularities in the microstructure influences the service time of the material, and consequently of the engine. The risk of failure by fracture or fatigue requires, that components fabricated from the superalloys are of the highest integrity, so that inspection and life time prediction are critical to ensure ongoing operation. These irregularities typically present in casting components are: pores, carbides, precipitates, and inclusions. In the specific case of directionally solidified (DS) components, some recurrent crystallographic defects, representing a weakness for the material, can be identified. In Fig.1.1 one can see how a DS microstructure looks like: the columnar grains are all oriented along the solidification direction. Deviations from this structure are considered as the relevant defects in above defined sense that reduce performance of the component. These deviations are:

- *Freckle chains*: long chains of equiaxed grains preferentially located at the component's surface [1] (Fig.1.2).
- *Foreign grain*: grain that nucleates spontaneously in any position of the component, deviating from the DS structure [2] (Fig.1.3).
- *Inclined grain boundary*: grain boundary with high inclination with respect to the solidification direction (Fig.1.4).
- *Transverse grain boundary (TGB)*: grain boundary with perpendicular orientation relative to the solidification direction (Fig.1.5).

All the mentioned defects have a different crystallographic orientation compared to the main one of the component. Their microstructure depend on process parameters and on the dimension of the component. Accordingly, it is interesting to understand how this misorientation between grains affects the strength of the material. And also, how the strength changes close the grain boundary if it is perpendicular or inclined with respect to the loading direction.

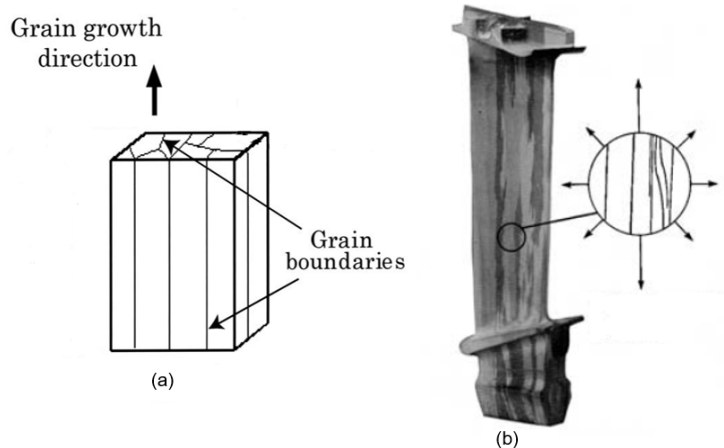


Figure 1.1: (a) Schematic drawing of an ideal directionally solidified microstructure [3], (b) Micrograph of an etched directionally solidified blade and a magnifications with the sketch of its columnar grains [4].

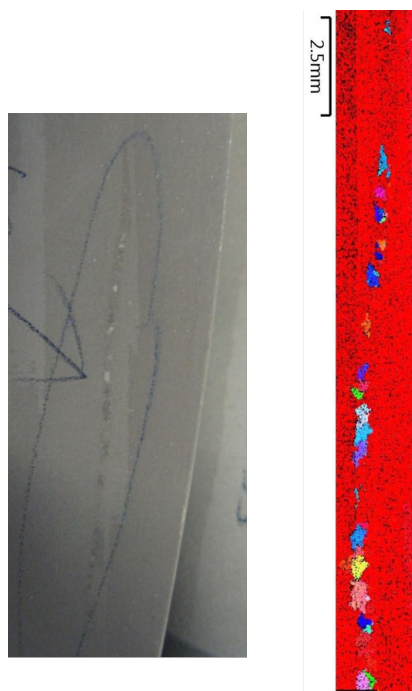


Figure 1.2: Micrograph and EBSD analysis of a Freckle chain on vane made of MAR M 247. The EBSD analysis make possible to observe the main crystallographic orientation of the mentioned component (in red) and the equiaxed grains of the Freckle chain with different crystallographic orientations (and consequently colors different from red) [2].

For Nickel-based superalloys and their applications in the aeronautical field for the realization of aero engines components, as it happens for almost any application in the field of structural materials, it is fundamental to be as much conscious as possible about what kinds of defects are present, where they are located, and how much they can limit the performance of the material in use.

As a consequence, it is very important to think about the fatigue life of the



Figure 1.3: Foreign grain marked on a component, made of MAR M 247, visualized after etching. The Foreign grain is spontaneously nucleated on the surface of the component during solidification. The different crystallographic orientation is clearly visible due to the different colors between the grain marked with the white circle and the remaining part of the component [2].

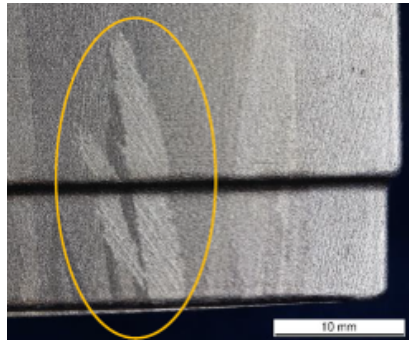


Figure 1.4: Inclined grain boundary on a component made of MAR M 247, visualized after etching. The different crystallographic orientation is clearly visible due to the different colors between the grain marked with the yellow circle and the remaining part of the component [2].

material. Most of the components in an aircraft engine are affected by cyclic loads and often high temperatures. As well know from literature, the life of the material under these conditions is highly dependent on the material's mechanical properties itself and the operational conditions (load amplitude, temperature, duration of the applied load, etc.) [5, 4, 6]. M. Smid & coworkers, in 2014 started looking at the role of defects in fatigue damage mechanisms of cast polycrystalline alloy MAR M 247 [7] (a description of the mentioned material is given in *Chapter 2*). They discovered that the factors that play the biggest role in the fatigue strength of material are grain size, grain orientation as well as size and distribution of casting defects like pores. The same research group, in 2015 focused on the influence of casting defect size on fatigue life, again for alloy MAR M 247 [8]. This study has been done applying the Murakami's statistical method using *Largest Extreme Distribution Theory (LEVD)*[8]. This theory is able to predict the biggest defects which can occur in a given volume, to compare them with the ones present on the fracture surface of the failed specimens. The theory is based on the evaluation of the

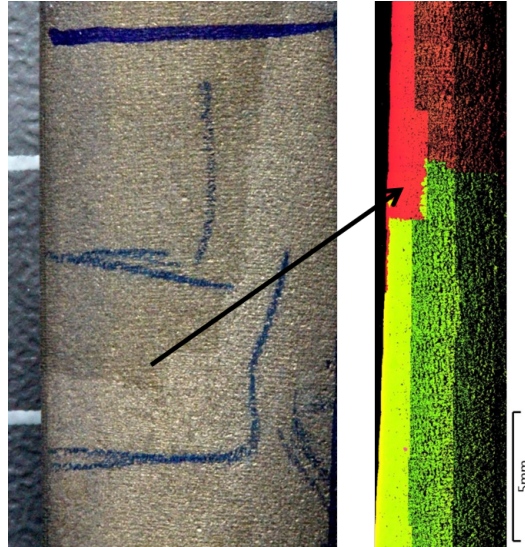


Figure 1.5: Micrograph and EBSD analysis of a transverse grain boundary (TGB). The different crystallographic orientation is clearly visible due to the different colors of the grains in the EBSD analysis. [2].

size of the largest defects on a controlled area S_0 (field of view). The measurement has to be done on n number of the controlled areas. The number of the controlled areas has to be sufficient for reasonable statistical description. The number of the measurements, on each controlled area, is dependent on specimen size and on chosen magnification. By proceeding in this way, they found a good agreement between the predicted and the real defect size, and that the specimens with the largest predicted defect size have the shortest fatigue life and vice versa [8].

A similar approach has been carried out by H. Tang and H. Guo in 2017 [9]. They were interested in the weakening effect of grain defects generated at geometric discontinuities of single crystal (SC) materials. For the experiments, a bicrystal specimen has been used. The sample has been analyzed with the finite element software Abaqus. As a result of this study, they understood that the yield strength and elastic modulus of misoriented grains have a significant effect on the stress distribution of the bicrystal model.

All the mentioned results confirm how important it is to take into account all these defects and irregularities, to study and define in an accurate way the properties of the material and its behavior in service.

What we know is, that fatigue crack nucleation is dependent on the local microstructure of the material, the internal stress distribution and the external loading conditions [10]. Cracks propagate if adjacent grains are favorably oriented for crack propagation or if the crack nucleus is large enough. H. Vehoff et al., in 2004, suggested a way to proceed in order to understand the role of these factors on fatigue crack nucleation at interfaces in bicrystals in Fe-3 wt.% Si [10]. Under high cycle fatigue (HCF), they compared the results coming from the experiments with the ones obtained by a finite element analysis. In particular, polycrystalline samples have been used for HCF tests. Then, using the EBSD (Electron back scattering diffraction) characterization technique, local orientation maps with grain size and orientation of adjacent grains have been created for these specimens. Another pa-

parameter considered was the grain boundary inclination. This data has been used as an input for the FEM analysis. From their results it is visible, that the stress is higher along the boundary and highest at the corner of the specimen. This is in good agreement with the experiments: the crack initiated at this corner and moved along the front surface before it started to propagate. Another result achieved by this study is, that the grain boundary inclination affects the stress field as strong as the the grain orientation [10]. Thanks to the OIM (orientation imaging) pattern, they were able to assert that stresses develop relatively fast at the boundary and rarely exceed the applied stresses by a factor of 2 [10].

Another situation, where the grain boundary shows how much impact it has on the mechanical properties of the materials, is the one described by L.L. Li and others [11]. Here, a Cu bicrystal specimen with a grain boundary inclined at 45° with respect to the loading direction, has been analyzed. This sample has been compared with a single crystal of same orientation as its component grain, after performing fatigue tests in a load controlled mode on both of them. From this study it is clear that the existence of the inclined grain boundary induces higher strain localization and early intergranular fatigue crack of the bicrystal specimen [11].

A similar research has been done at *MTU Aero Engine*. The first approach consisted in the estimation of life reduction factors for grains structure defects using simple calculation methods [12]. Then, following the same method used by H. Vehoff and others [10], another project work was started by Ing. M. Fried and Ing. F. Vöse at MTU Aero Engines. In this case, the tasks are to carry out a systematic investigation on typical grain structure defects, improving the experimental database, and enriching the study with the development of FEM calculations, in order to make life assessments more reliable and less conservative.

1.2 Objective of the master thesis

The focus of this master thesis is on the effect of misorientation and grain boundary inclination on fatigue. The goal is to understand how they affect the performance of the material in order to develop fatigue life prediction of components. The material analyzed in detail is the Nickelbase superalloy MAR M 247, that can be used as polycrystal, DS and single crystal material (for further details, see next sections: *Chapter 2*).

The thesis is organized into two main parts:

1. *Experiments and documentation*: analysis of LCF experiments, conducted on specimens with known geometry and crystallographic parameters, is to be done. A characterization of the fracture surfaces of samples has been performed using *Scanning Electron Microscope (SEM)*, to find the exact crack initiation point, and *Electron Backscatter Diffraction (EBSD)*, to determine the exact crystallographic orientation of the specimens and their actual grain boundary inclination (*Chapter 4: Experiments*).
2. *Finite-Element Modelling*: in this part, a 3D-model with the desired geometry and mechanical properties, will be firstly drawn and then tested with a specific script that can reproduce the experimental conditions. The obtained results

have been compared with the ones coming from the experiments. Calculations with selected values of grain boundary inclination and crystallographic misorientation are also performed to directly study their influence on the material properties (*Chapter 5: Simulations*).

Chapter 2

Material

2.1 General Properties

Nickel-based superalloys are complex and widely used materials for hot parts [6]. They are developed to fulfill the following properties [6]:

- High temperature strength
- Toughness
- Resistance to degradation in corrosive or oxidizing environments
- Creep rupture strength
- Excellent high- and low-cycle fatigue resistance

For these reasons, they are used for several applications that involve severe operating conditions. As is the case of aircraft and power generation turbines, rocket engines, nuclear power and chemical processing plants.

It is well known, that the microstructure and the composition of the alloy are deeply important and effective on the properties of the materials required for a specific application [6, 4, 13]. Accordingly, the fabrication process change dependently on what you want to produce and obtain. Blades and vanes are usually produced by investment casting procedures. Since grain boundaries are potential sites for damage accumulation at high temperatures, the blades in the first stages of the turbine are typically single crystals, whereas the blades in cooler subsequent stages of the turbine are fabricated from conventionally cast equiaxed alloys. In Fig. 2.1 these different configurations are presented. In some cases, vanes and blades are produced as directionally solidified (DS) components. There are at least two reasons that can justify this way to proceed [6]:

1. The grain boundaries are oriented parallel to the applied-stress direction, enhancing in that way the creep-rupture resistance location.
2. DS process provides a preferred low-modulus $\langle 001 \rangle$ texture or orientation parallel to the solidification and centrifugal loads direction. This increases the thermal fatigue resistance.

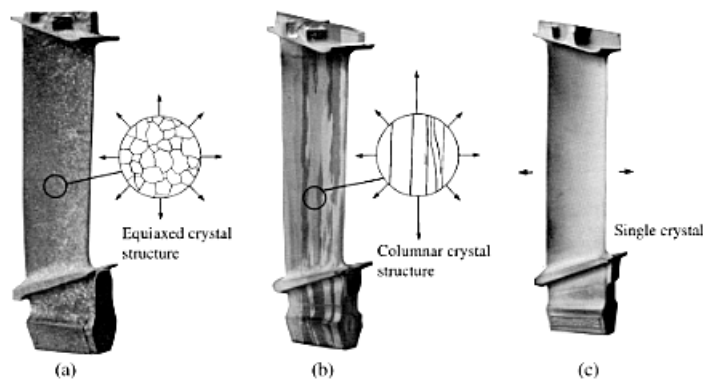


Figure 2.1: Examples of blades with different grain structures: (a) Polycrystalline, (b) Columnar grains, (c) Single crystal [13].

2.2 Composition and Microstructure

The chemical composition of a Nickel-based superalloy is usually complex. A minimum number of 12-13 elements is included and carefully controlled. The most of the Nickel alloys contain 10-20% *Chromium*, up to 8% *Aluminum* and *Titanium*, 5-10% *Cobalt*, and small amounts of *Boron*, *Zirconium*, and *Carbon*. Optional common additions are *Molybdenum*, *Tungsten*, *Columbium*, *Tantalum*, and *Hafnium*. Each of these elements has a specific effect on the overall properties of the material. As

IIA	III.A	IV.A							
	B	C							
	Al								
			IVB	V.B	VI.B	VII.B	← VIII.B →		
			Ti	V	Cr		Fe	Co	Ni
	Y	Zr	Nb	Mo			Ru		
		Hf	Ta	W	Re				

Figure 2.2: Important elements in the constitution of nickel-based alloys [14].

shown in ??, there are 3 main classes of elements:

- *I class*: elements that stabilize the face-centered-cubic (FCC) austenitic (γ) matrix. It is the case for elements like Ni, Co, Fe, Cr, Mo, and W (so elements from Groups V, VI, and VII).
- *II class*: elements that contribute to the formation of γ' precipitate Ni_3X . These elements are Al, Ti, Nb, Ta, and Hf (elements from Groups III, IV, and V).
- *III class*: elements that segregate at the grain boundary. They are B, C, and Zr (coming from Groups II, III, IV).

Alloy MAR M 247 is a special kind of second generation nickel-base superalloy [15] due to its ability to appear in different configurations. In fact, it is possible to find this alloy as a polycrystalline (PC), as a directional solidified (DS), and as a single crystal (SC) material. This alloy has been developed by Martin Marietta Corporation [7]. The usual technology applied to this material is the investment casting, but directional solidification techniques can also be used to increase the creep rupture strength of the material. For its specific characteristics, alloy MAR M 247 can be considered as an advanced cast superalloy with an excellent high temperature strength, corrosion and oxidation resistance.

Ni superalloys typically consist of a matrix γ , coherently embedded strengthening precipitates of a γ' ordered intermetallic phase and carbides. In the case of MAR M 247, the γ' volume fraction is around the 60%, and this provides good mechanical properties at high temperature [16].

The main alloying elements of MAR M 247 are reported in the matrix below (wt%) (Tab.2.1):

Table 2.1: M 247 composition [17].

C	Al	Co	Cr	Hf	Mo	Ta	Ti	W	Ni
0.15	5.42	9.91	8.37	1.37	0.67	3.05	1.01	9.92	Rest

It is possible to define and describe the major phases present in this superalloy, and generally in every kind of Ni-based superalloy, in the following way [6]:

1. γ *Matrix*: a continuous FCC phase with high percentage of solid solution elements. It consist principally of Ni, Co, Cr, and refractory elements such as Mo and W.
2. γ' : precipitates with a $L1_2$ crystallographic structure consist preferentially of Al/Ti and Ni as Ni_3X . This phase precipitates coherently with the matrix and its shape changes as a function of the matrix-lattice mismatch (for a lattice mismatch of 0-0.2% γ' has a spherical shape and a cubic one for the range 0.5%-1.0%; if the mismatch is higher than 1.25%, the γ' precipitates become plates).
3. *Carbides*: carbon combines with reactive and refractory elements such as Ti, Ta, Hf to form MC carbides that during heat treatments decompose and generate $M_{23}C_6$ and M_6C . Usually, they can be found at the grain boundary and their shape is plate-like or globular or Chinese script.
4. *Borides*: rare grain boundary particles.

Samples cut directly from a vane, that was made of the same material used for the experiments, have been analyzed to directly observe what has been just described.

Firstly, an EBSD characterization, along three different directions X-Y-Z, allowed to observe the number of grains presents and the relative misorientation between them (Fig.2.3, Fig.2.4, Fig.2.5). In Fig.2.6, using a color scaling, it is possible to see the grain orientation distribution for the specific vane section. In the X and Y direction the grains are more or less arbitrarily oriented, whereas in the Z direction they are mostly oriented in the $\langle 001 \rangle$. As a result of this EBSD characterization, it was possible to estimate the mean Euler angles (E_1, E_2, E_3) defining the

orientation of each grain (Tab.2.2) [18]. E_1 corresponds to the angle rotated about the Z-axis, E_2 about the new X-axis (after the first rotation), and E_3 about the new Z-axis (after the second rotation). The mentioned reference system is shown in Fig.2.3, 2.4 and 2.5.

Table 2.2: The Euler angles.

Grain	$E_1(^{\circ})$	$E_2(^{\circ})$	$E_3(^{\circ})$
1	6.44	16.79	23.73
2	359.29	19.72	56.43
3	12.95	16.64	20.07
4	356.52	16.61	75.37
5	11.61	14.76	33.23
6	1.43	15.97	48.34
7	5.26	12.68	15.05
8	13.41	20.57	42.16

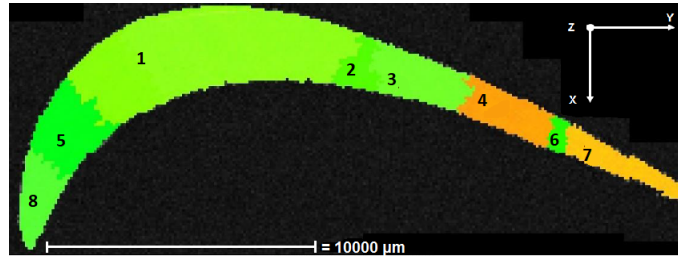


Figure 2.3: EBSD-coloring according to inverse pole figure in X-direction [2]. The reference coordinate system is reported here.

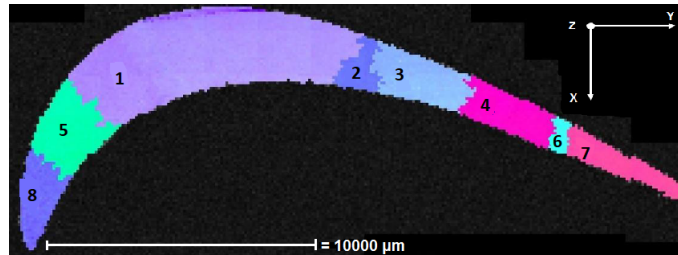


Figure 2.4: EBSD-coloring according to inverse pole figure in Y-direction [2]. The reference coordinate system is reported here.

Through SEM analysis, it was possible to identify the phases γ (white) and γ' (black) (Fig. 2.7), and also to evaluate the γ' fraction. The fraction of γ' has been determined after studying one particular grain at three different locations, and collecting the data coming from the *backscattered-electrons* (BSE) and the *secondary electrons* (SE). From each position, a γ' fraction has been calculated. The mean value is $\sim 54\%$ (Tab. 2.3). Normally, γ' has to be around the 60% [8]. In that case, the explanation for this lower amount can be easily found. Looking carefully at Fig. 2.7, it is possible to notice that there are areas where the γ' phase has not been correctly detected (areas marked with the red circle). In fact, these areas have a shades of gray that cannot be recognized by the software. This led to a

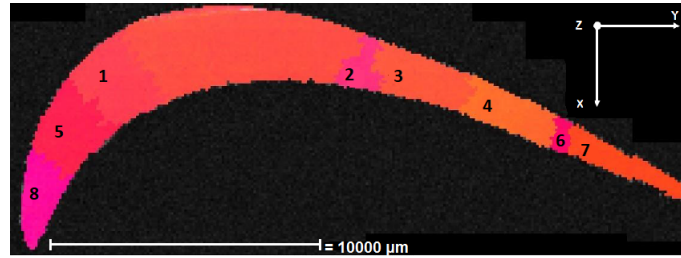


Figure 2.5: EBSD-coloring according to inverse pole figure in Z-direction [2]. The reference coordinate system is reported here.

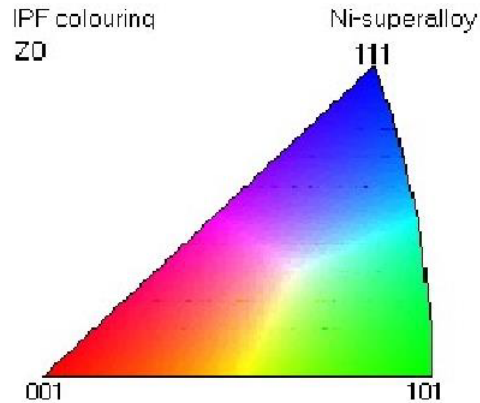


Figure 2.6: Color scaling representing the grains orientations' distribution [2].

percentage of that phase lower than expected. A solution for this kind of situation can be the removal at these areas from the total one considered for the estimation. A further analysis can be done, concerning the carbides presence in the alloy. For

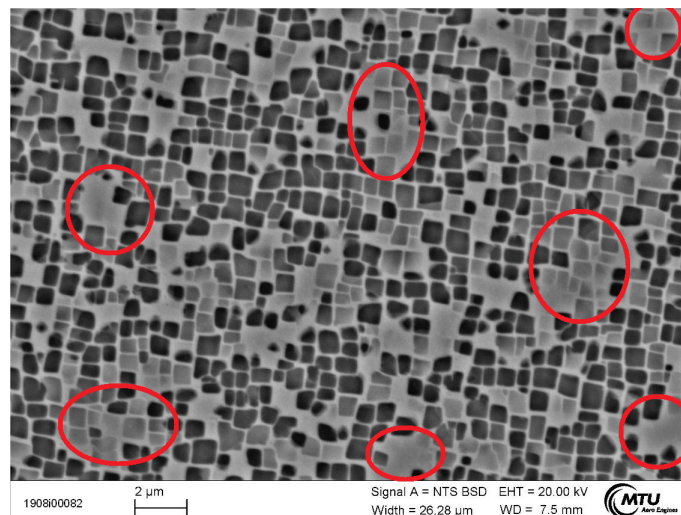


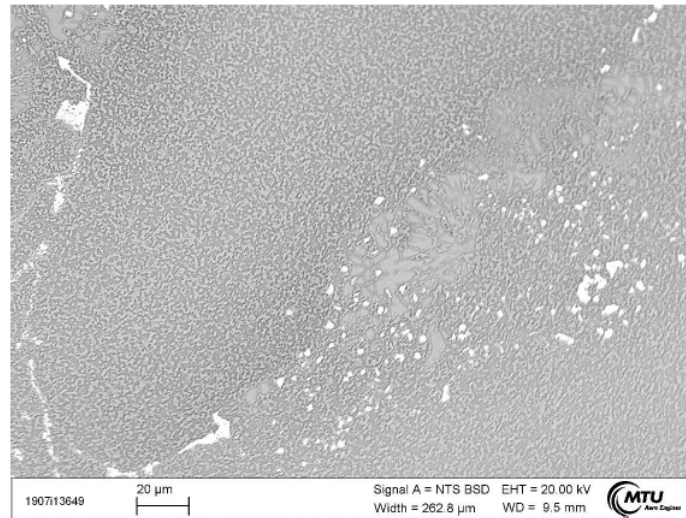
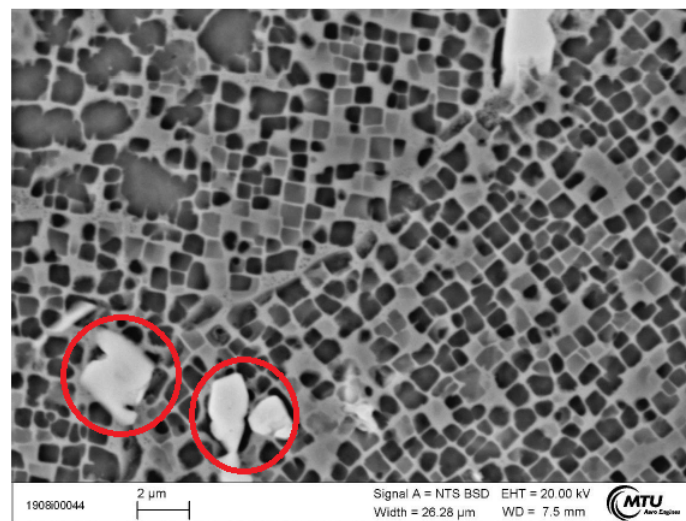
Figure 2.7: γ/γ' in dendritic core within a grain [2].

that purpose, another sample of MAR M 247 was analyzed by SEM, in particular analyzing Back-scattered electron (BSE). Before the characterization, the sample has been etched using molybdic acid. As expected, the carbides are located at the

Table 2.3: The γ' fraction [2].

Position within dendrite core	γ' fraction (%)
1	~ 50
2	~ 55
3	~ 57
Mean	~ 54

grain boundary or close to it (Fig.2.8, Fig.2.9). The carbides have a variable shape and dimension.

**Figure 2.8:** BSE analysis of carbides at the grain boundary [2].**Figure 2.9:** SE analysis of carbide at the grain boundary [2]. Carbides circled by red marks.

2.3 Casting defects

In casting materials, the presence of defects like pores and inclusions is inevitable. Important parameters that must be taken into account, are defects size and distribution, which also depend on the casting conditions. Casting defects cause stress concentration, and often coincide with crack initiation sites. The amount of pores size can be reduced by specific technologies like HIP (Hot Isostatic Pressing). In Fig.2.10 it is possible to see, that defect size and fatigue life are inversely proportional: as much as the first increases, the second starts decreasing. Additionally,

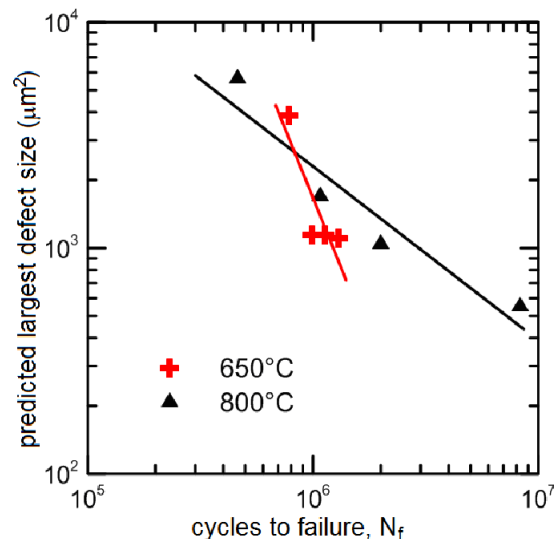


Figure 2.10: Correlation between predicted defect size and obtained life-time [8].

several types of grain defects may develop during the solidification process. As mentioned already in (*Chapter 1: Introduction*), the most common grain defects in DS alloys are:

- Freckle chains
- Foreign grains
- Inclined grain boundary
- Transverse grain boundary

All the mentioned grain structure defects may be harmful for fatigue life since they represents stress concentration points.

Freckles chain Freckle-type defects arise because of convective instabilities in the mushy zone that develop as a result of density inversions created by progressive segregation of individual alloying elements during solidification. The fluid flow within “channels”, that develops because of these instabilities, results in fragmentation of dendrite arms, producing a small chain of equiaxed grains aligned approximately parallel to the solidification direction. Freckles are enriched in elements that segregate to the interdendritic (as Re, Ti, W [19]) region during solidification, and thus differ in composition from the base alloy. Freckle formation is promoted by low

cooling rates (low thermal gradients), and corresponding large dendrite arm spacing for a fixed alloy composition.

Foreign grains Foreign grains differ from freckles in size and because they have the same nominal composition as the base alloy. However, they are typically larger and elongated along the solidification direction. To prevent the formation of foreign grains, a careful control of heat transfer has to be done. In particular, the solidification rate R has to be lower than:

$$R = \frac{K_T G_s}{\Delta H} \quad (2.1)$$

If R is higher than the number indicated by eq.2.1, then equiaxed grains will be formed [6].

Inclined and transverse grain boundaries These kind of grain structure defects are typical for DS components. They are formed during the solidification process as a consequence of the mutual interference of the single columnar grains due to the different growth rate .

Chapter 3

Fatigue

Fatigue is the progressive weakening of a material, caused by a cyclic load that induces a localized damage, and consequently, the growth of cracks. If the loading is high enough, each loading cycle will let the crack grow by certain amount. When the crack reaches a critical size, it starts propagating rapidly until the final failure of the component. It is possible to define 3 steps for that process:

1. *Crack initiation*: crack formation due to the movement of dislocations (3.1), coalescence of vacancies that forms pores, inclusions or even manufacturing defects [20].
2. *Crack propagation*: each load cycle acts opening the crack and increasing its dimension (the presence of pores, inclusions and carbides may influences the velocity of crack propagation). This phase is clearly detectable on the fractured component because of the striations, signs that marks the propagation of the crack.
3. *Final failure*: the critical dimension for the crack is reached and the remaining section of the component is not enough anymore to sustain the applied load.

A typical example of a fatigue crack surface is shown in Fig.3.1.

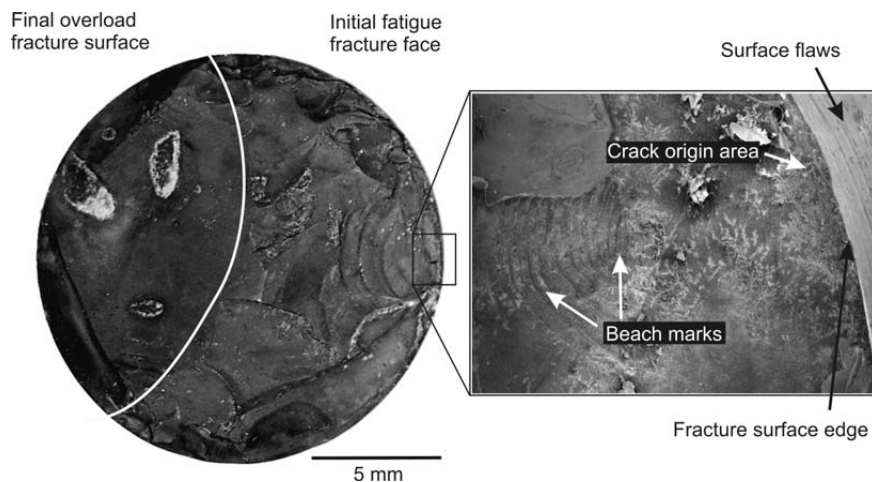


Figure 3.1: Example of a fracture surface of a fatigue failure showing the striations [21]. The crack propagates from the crack initiation point until the final overloaded fracture surface.

Specific kind of tests are available to measure the materials behavior under fatigue conditions. In particular, it is possible to distinguish between high-cycle fatigue (HCF) and low-cycle fatigue (LCF). The difference has to do with plastic and elastic strain. LCF is usually characterized by repeated plastic deformation (i.e. in each cycle), whereas HCF is characterized by elastic deformation. An alternative definition is that which provides for the distinction between LCF and HCF based on the number of cycles. A typical threshold value is $10^4 - 10^5$ cycles [22].

In this work the attention has been focused on LCF tests.

In order to perform fatigue tests, two main parameters have to be defined: the maximum applied stress (σ_{max}), the minimum stress (σ_{min}), and the strain ϵ in case of strain controlled mode tests. Based on them, other variables are defined, as the stress amplitude (eq.3.1) and stress range (eq.3.2):

$$\sigma_a = \frac{(\sigma_{max} - \sigma_{min})}{2} \quad (3.1)$$

$$\sigma_r = \sigma_{max} - \sigma_{min} \quad (3.2)$$

To set the experimental conditions, one of the most important parameters is the R-factor, defined as in eq.3.3:

$$R = \frac{\sigma_{min}}{\sigma_{max}} \quad (3.3)$$

One possible situation is, that the test specimen starts out unloaded (zero stress), it is loaded to the required maximum positive stress level, and then unloaded to start the next cycle. In this case, the R ratio would be exactly zero. Another situation is settled when the minimum stress is the negative of the maximum stress. In this case, R ratio is exactly equal to -1. This is known as fully reversed ($R=-1$) testing.

Fatigue properties of materials are often described using the *S-N curve* or *Wöhler curve*. This curve shows the relation between e.g. the stress amplitude and number of cycles to failure (horizontal axis given on logarithmic scale). On the vertical axis (either linear or logarithmic) the stress or strain amplitude is given (Fig.3.2).

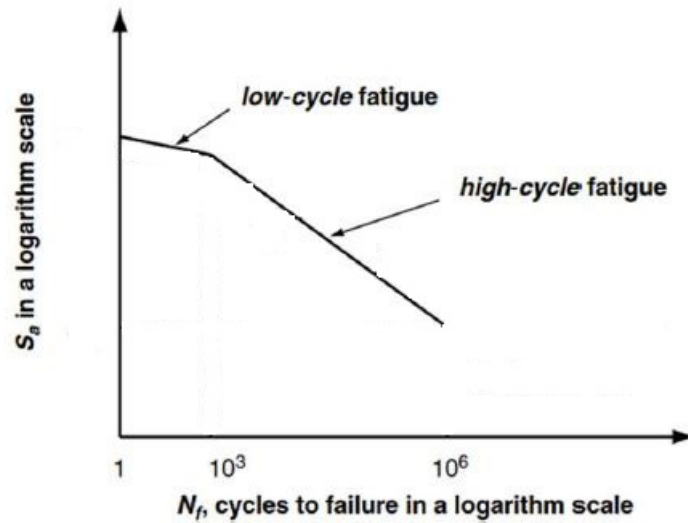


Figure 3.2: Example of a Wöhler curve, adapted from [23]. The value of N_f can be used to distinguish between low and high cycle fatigue, respectively represented by two different slopes for the curve.

Chapter 4

Experiments

4.1 The specimen

For the success of the experiments, and in order to obtain results describing exactly the desired conditions, the properties of the specimen are important.

The starting point is a bicrystal plate, having the desired crystallographic misorientation and grain boundary inclination between the two grains. This plate is produced using the directional solidification technique, with two different seed selectors located at the extremity of the plate, corresponding to the two mentioned grains. The solidification direction is $\langle 001 \rangle$. One of the two grains, *Grain1*, has a standard secondary orientation, kept constant in all the different configurations of the specimens. This orientation is $\langle 010 \rangle$. The secondary orientation of the second grain, *Grain2*, can take different values, resulting in three different possible misorientations (φ) looking in the loading direction: 16° , 32° , and 45° (*Grain2*). This misorientation, also named as primary misorientation, represents the deviation of the two grains from the loading direction. A sketch of the plate, with the described features, is shown in Fig.4.1. Then, a machining operation is executed on the plates to produce the *blanks*, and subsequently, with a second machining operation, the samples in their final shape. After cutting the blanks, they are etched, to detect the exact position of the grain boundary (Fig.4.2). The solutions used for the etching is composed by H_2O , HCl and H_2O_2 . Finally, the blanks are ready to be machined. The specimens obtained have the geometry shown in Fig.4.3, and their final shape is given in Fig.4.4. As clear from Fig.4.4, the grain boundary is marked on the specimen. This mark is necessary to put the strain gauge for the tensile testing in the exact position that allows to include, in the gauge section, 50% of *Grain 1* and 50% of *Grain 2*. The length of the gauge section is 18 mm.

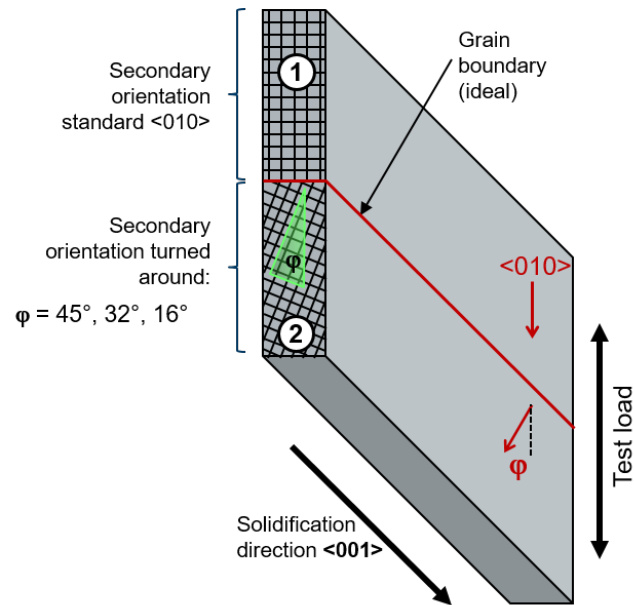


Figure 4.1: Sketch of the bicrystal plate used to obtain the specimens [2]. The solidification direction ($\langle 001 \rangle$) is the same for the two grains. Their misorientation is represented by the values of φ that can be 16° , 32° or 45° . The loading direction is coincident with the orientation of *Grain 1*: $\langle 010 \rangle$.

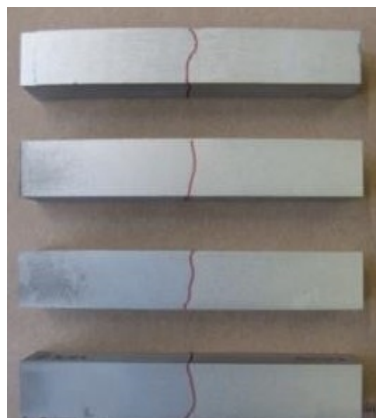


Figure 4.2: Blanks after etching [2]. The red lines represent the grain boundary between the two grains.

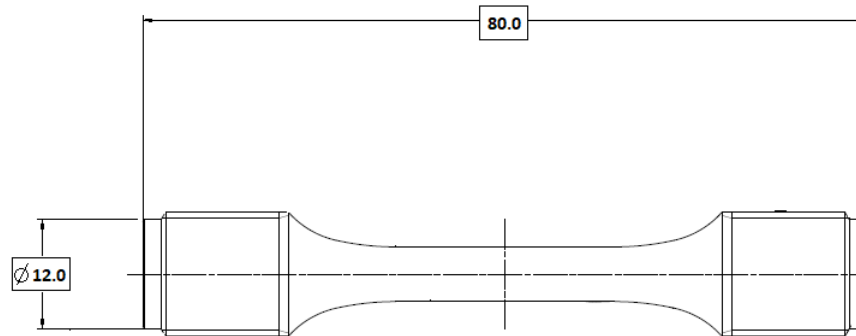


Figure 4.3: Adapted technical draw of tested LCF specimen [2]. Dimensions given in millimeters.

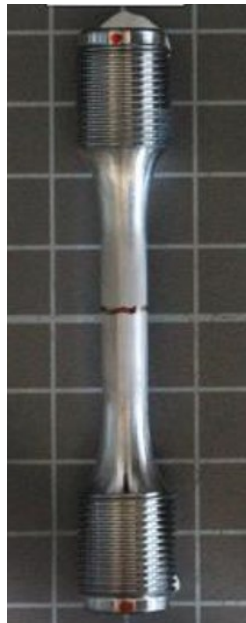


Figure 4.4: Final shape of the LCF specimen [2].

4.2 Testing conditions

The specimens have been tested under low cycle fatigue in strain controlled mode, and with $R = -1$. The test speed was 0.3%/s with a triangular loading waveform. The temperatures considered are 600°C and 980°C. For each temperature, two different strain amplitudes (ϵ_a) have been imposed.

An overview of all the tested specimens, and the specific testing conditions such as the primary misorientation (φ), the grain boundary inclination (α), and the strain amplitude ϵ_a is given in Tab.4.1 for 600°C, and in Tab.4.2 for 980 °C.

Sketches of the mentioned bicrystal specimens are shown in Fig.4.5. The results

Table 4.1: Bicrystal specimens, 600°C.

Sample	φ (°)	α (°)	ϵ_a (%)
1_BC_600	32	50	0.5
2_BC_600	32	50	0.4
3_BC_600	45	0	0.5
4_BC_600	45	0	0.4
5_BC_600	45	0	0.5
6_BC_600	45	0	0.4
7_BC_600	32	0	0.5
8_BC_600	32	0	0.4
9_BC_600	32	45	0.5
10_BC_600	32	45	0.5
11_BC_600	16	0	0.4
12_BC_600	16	0	0.5

Table 4.2: Bicrystal specimens, 980°C.

Sample	φ (°)	α (°)	ϵ_a (%)
1_BC_980	45	0	0.3
2_BC_980	45	0	0.2
3_BC_980	32	45	0.3
4_BC_980	45	45	0.2
5_BC_980	45	0	0.3
6_BC_980	45	0	0.2
7_BC_980	32	0	0.3
8_BC_980	32	45	0.2
9_BC_980	16	0	0.2
10_BC_980	16	0	0.3
11_BC_980	16	0	0.3
12_BC_980	32	0	0.3

coming from the described experiments have been compared with the ones of the single crystal samples, tested in the same conditions (Tab.4.3 and Tab.4.4).

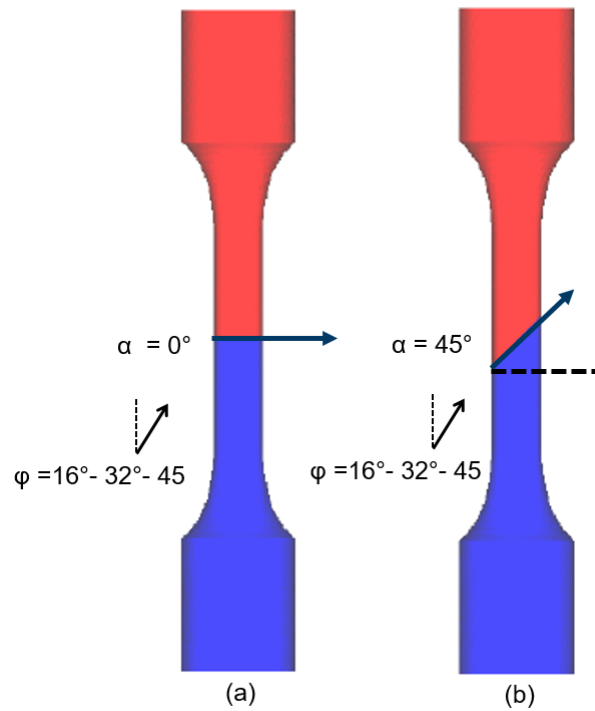


Figure 4.5: Sketches of samples having $\alpha = 0^\circ$ (a), and $\alpha = 45^\circ$ (b). The misorientation φ can have each of the indicated values; adapted picture from [2].

Table 4.3: Single crystal specimens, 600°C .

Sample	ϵ_a (%)
1.SC.600	0.5
2.SC.600	0.5
3.SC.600	0.6
4.SC.600	0.6
5.SC.600	0.7
6.SC.600	0.8
7.SC.600	0.8

Table 4.4: Single crystal specimens, 980°C .

Sample	ϵ_a (%)
1.SC.980	0.3
2.SC.980	0.3
3.SC.980	0.4
4.SC.980	0.45
5.SC.980	0.5
6.SC.980	0.7

4.3 Results

In this section the results of the experiments introduced above are reported. Bicrystal specimens are here analyzed and compared with single crystal ones.

4.3.1 Strain

In Fig.4.6 and in Fig.4.7, the normalized percentage strain against the number of cycles to failure, in a logarithmic scale, it is plotted. The normalization has been done dividing all the percentage strain by the highest value between them. As already discussed, the experiments have been performed in strain controlled mode. For this kind of plots, the role of the stiffness is important: the differences between the specimens are also due to the values of the Young's modulus, that change as a function of the orientation. In the figures mentioned above, it is possible to see data referring to single crystal specimens in blue (the blue line is the power regression curve) and several colored points to representing the different types of bicrystal specimens. Looking at Fig.4.6, from the three series having the same value of the grain boundary inclination ($\alpha = 0^\circ$), it is possible to observe the effect of φ on the material properties. In fact, the number of cycles to failure increases as the primary misorientation decreases. That means, that for $\alpha = 0^\circ$, the highest number of cycles to failure is observed for $\varphi = 16^\circ$, and the lowest for $\varphi = 45^\circ$. This behavior does not change for different values of the normalized strain range. Moreover, keeping constant the value of the primary misorientation, for example $\varphi = 32^\circ$, and changing α , it is possible to see that a higher value of the grain boundary inclination reduces the life of the specimens. Another conclusion to be drawn from Fig.4.6 and Fig.4.7 is, that the life of bicrystal specimens, tested in a strain controlled mode, is lower than the life of single crystal specimens, tested under equivalent strain.

The same considerations can be done looking at Fig.4.7. Consequently, what has just been written is valid for both 600°C and 980°C .

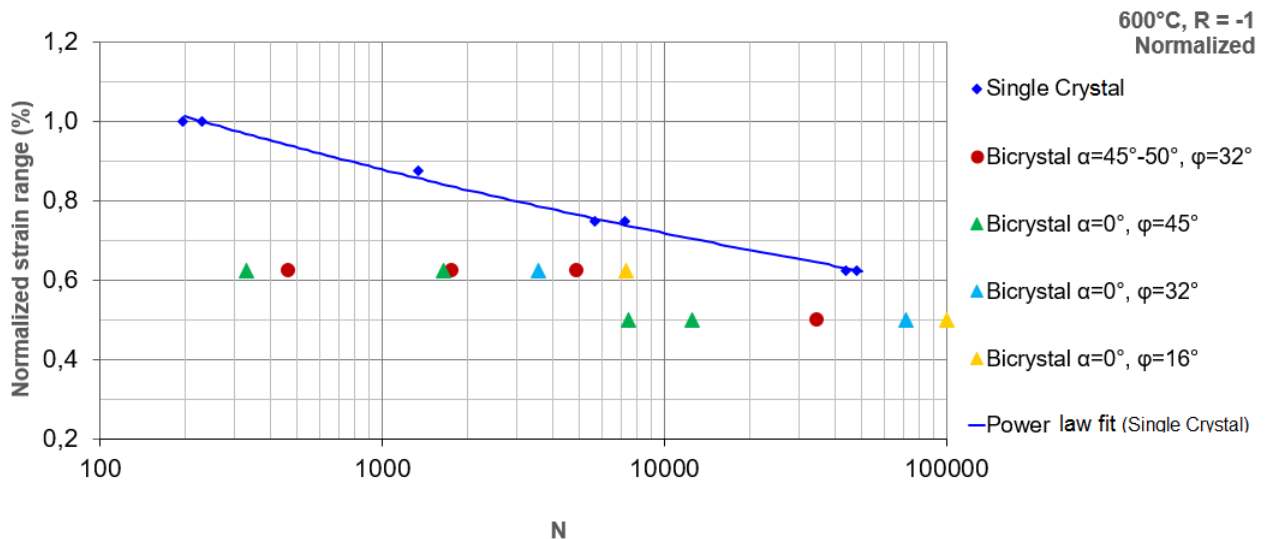


Figure 4.6: Normalized strain range against number of cycles to failure for specimens tested at 600°C .

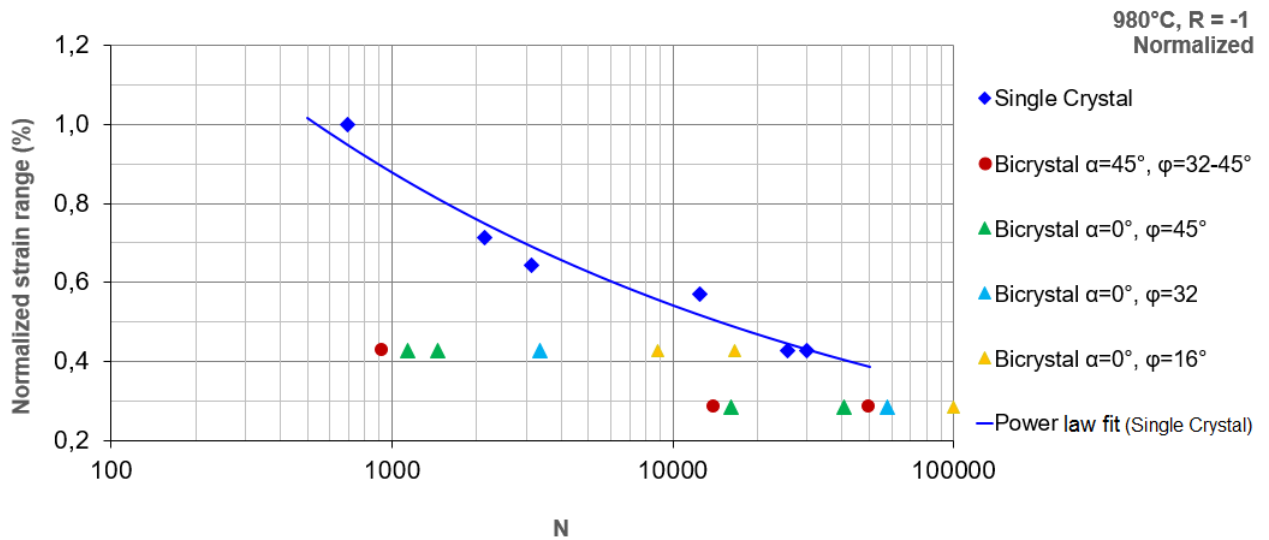


Figure 4.7: Normalized strain range against number of cycles to failure for specimens tested at 980°C.

4.3.2 Stress

Focusing on the stress, the effect of the E modulus is not directly visible anymore. In Fig.4.8, the results for single crystal and bicrystal specimens tested at 600°C

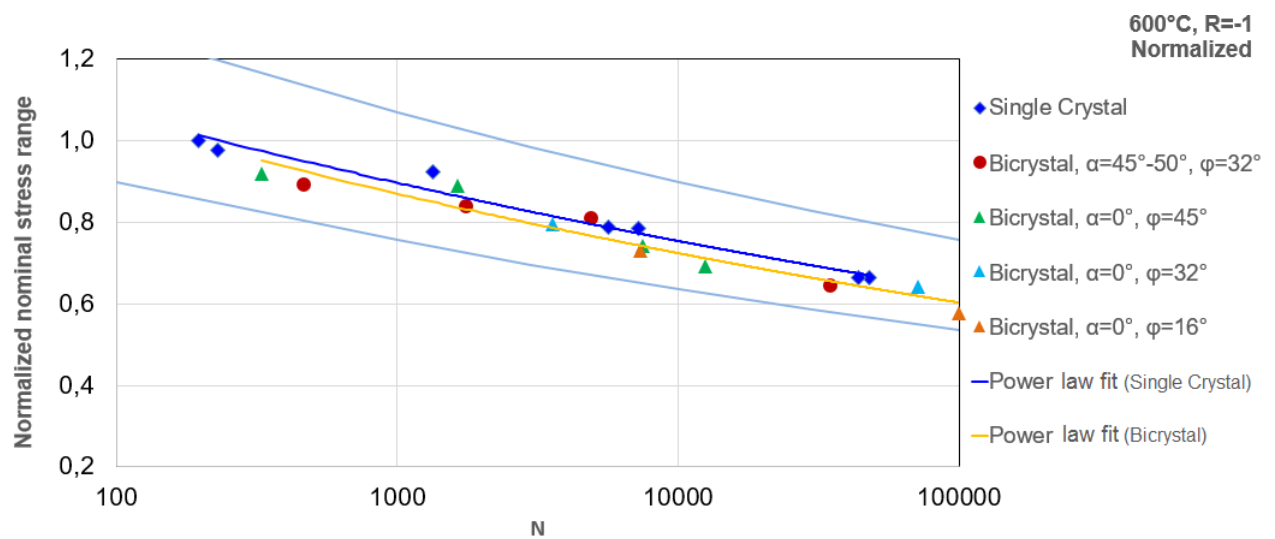


Figure 4.8: Normalized nominal stress range against the number of cycles to failure (600°C).

are collected. The same has been done in Fig.4.9 for samples tested at 980°C. On the axes of the graphs the number of fatigue cycles, on a logarithmic scale, and the normalized stress range are inserted. In these two graphs are shown the experimental points for the single crystals (blue points) and the associated mean power regression curve. As for the strain analysis, the bicrystal points correspond to symbols having different colors and shapes for different series of specimens. The yellow curve is the mean power regression curve for the bicrystals. Considering Fig.4.8, one notes a

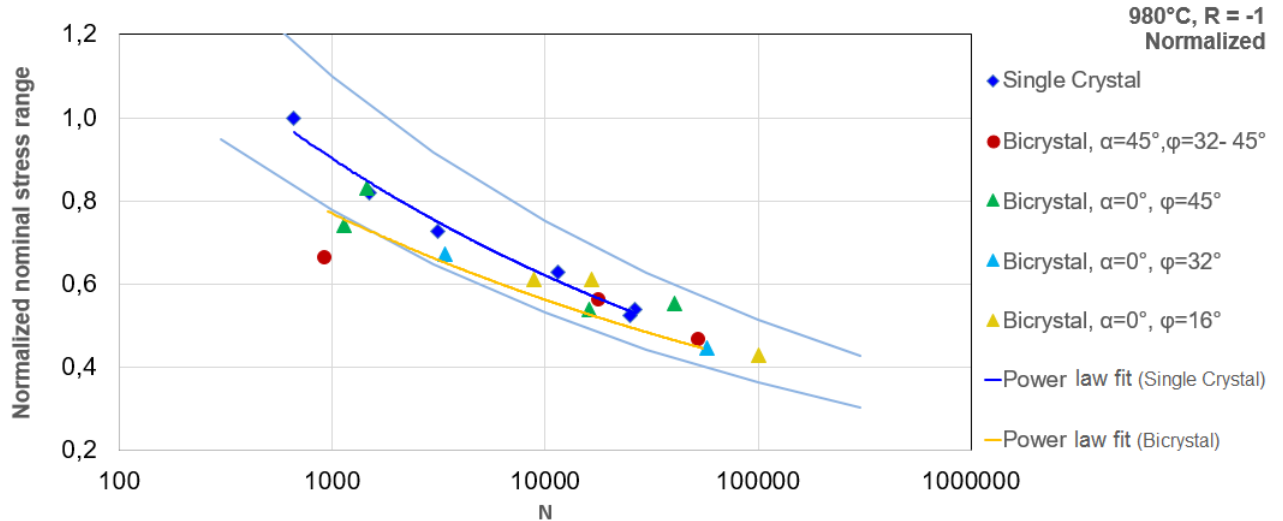


Figure 4.9: Normalized nominal stress range against the number of cycles to failure (980°C).

good agreement between single crystal and bicrystal is present. In fact, the yellow and the blue curve are quite close to each other. Moreover, all the bicrystals points are located inside a scatter band obtained applying a factor of 3 to the normalized stress range. Also in this case, for $\alpha = 0^\circ$, the number of cycles to failure is reduced by the increase in value of φ . Instead, when the value of the primary misorientation is fixed, for example $\varphi = 32^\circ$, it is possible to see, for almost the same value of the normalized stress range, the number of cycles to failure is reduced for high values of the grain boundary inclination.

For a temperature of 980° C (Fig.4.9), these considerations are still valid. The most of the single crystal points are above the bicrystal ones. The bicrystal fall within the scatter band obtained as for 600° C. There is still a good agreement between the single crystals and the bicrystals, even if lower than the one observed at 600° C.

4.4 Characterization

After the experiments, the specimens were analysed by using specific characterization techniques.

In this case, SEM has been used to investigate the failure surfaces of the specimen, utilizing backscattered and secondary electrons. In that way, it was possible to find the crack initiation point and the cause of the failure. Moreover, an EBSD characterization has been done on some specimens to be able to find the Euler angles, that exactly define the primary crystallographic misorientation, and the exact grain boundary shape.

4.4.1 SEM

For the SEM characterization, one half of the specimen is observed at microscope. Firstly, the specimens have to be prepared for the analysis. This preparation consists

of a cleaning process divided into several steps. In each step, the selected half of the sample is immersed into several liquids, each for 5-7 minutes. The solutions used for the cleaning are listed here, already in the correct order:

1. Cold water
2. Tickopur
3. Acetone
4. Ethanol

This sequence has to be repeated twice.

When the cleaning process is completed, the half specimen is glued on a basement that will be directly inserted inside the microscope.

Some results for the single crystal specimens are shown in Fig.4.10 for 600°C, and in Fig.4.11 for 980°C.

In Fig.4.10, the fractured surfaces of single crystal materials is shown. The crack initiation surface is clearly visible (Fig.4.10.1), where the surface is smoother than in other locations. In the enlargement below (Fig.4.10.3), the crack initiation point is marked with a blue circular sign. In this particular case, the failure of the specimen is due to a pore with a dimension of $\sim 165 \times 380 \mu\text{m}$ and distance of $600 \mu\text{m}$ from the outer surface (Fig.4.10.2, red mark).

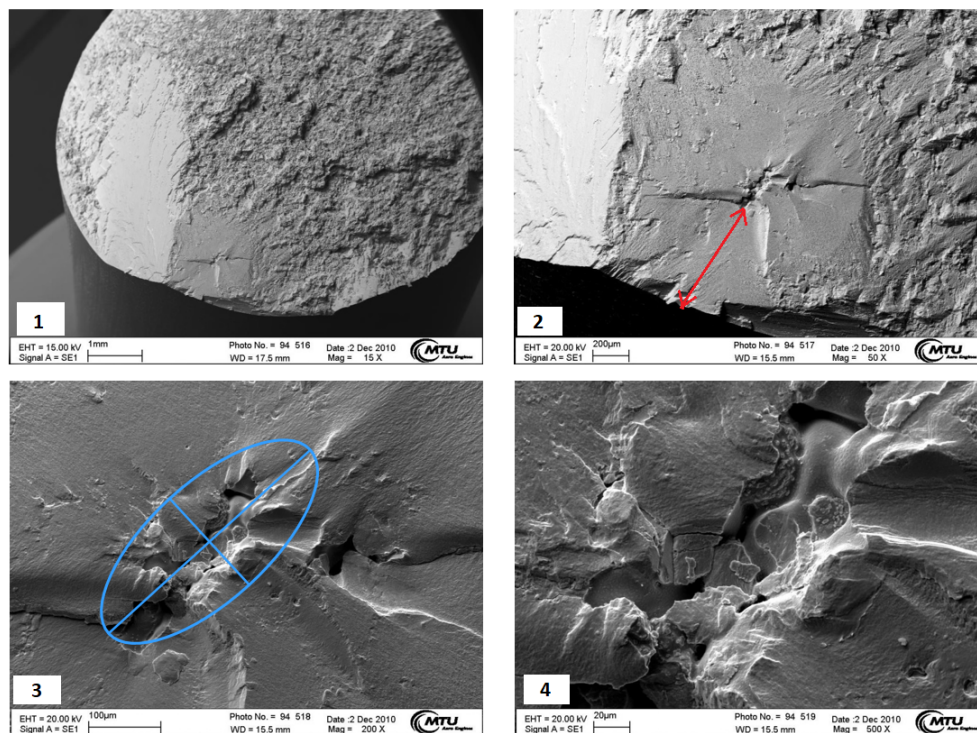


Figure 4.10: SEM characterization of the single crystal *Sample 2_SC_600*, (600°C); adapted picture from [2].

However, it is not always easy to found the crack initiation point. Situations like that are shown in Fig.4.11. Here, the surface appear very wrinkled and irregular.

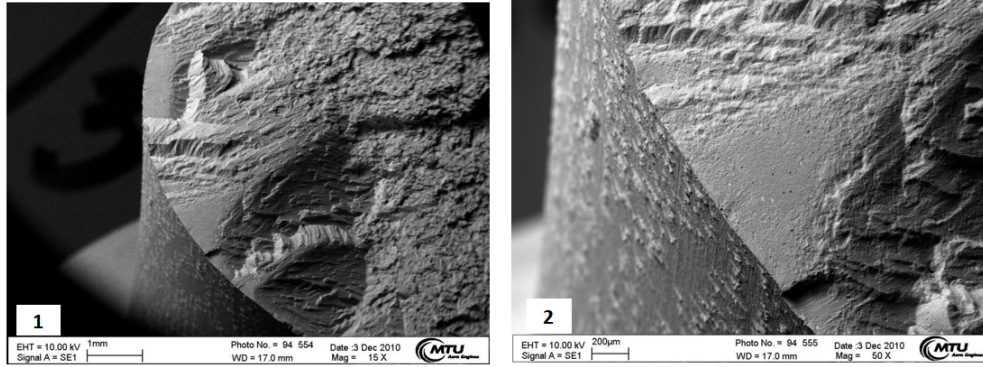


Figure 4.11: SEM characterization of the single crystal *Sample 1_SC_980*, (980°C); adapted picture from [2].

Nevertheless, it is possible to assert that at lower temperatures, for example 600°C, the cause of failure is usually a pore or a carbide, whereas at higher temperatures, like 980°C, the rupture of the sample can be explained as a consequence of oxidation. What just said, it is confirmed by the results obtained from the SEM characterization conducted on the bicrystal specimens. In Tab.4.5 and Tab.4.6 are mentioned the reasons of failure for the tested specimens, respectively at 600°C and 980°C.

Table 4.5: Cause of failure of bicrystal specimens tested at 600°C.

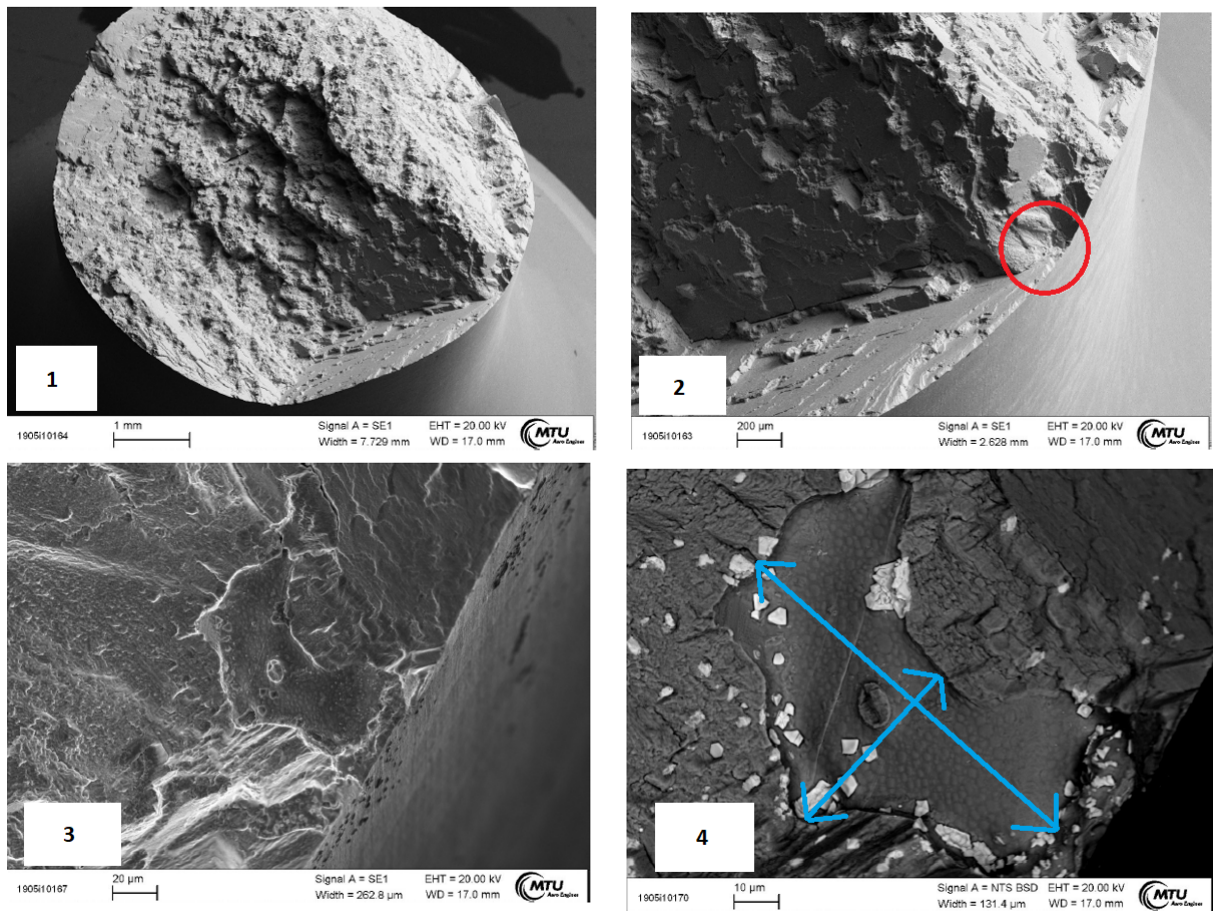
Sample	Cause of failure
1_BC_600	Pore
2_BC_600	Pore
3_BC_600	Carbide
4_BC_600	Pore
5_BC_600	Pore
6_BC_600	Pore
7_BC_600	Pore
8_BC_600	Pore
9_BC_600	Unidentified
10_BC_600	Carbide
11_BC_600	Not failed
12_BC_600	Pore

Another example of failure due to a pore is shown in Fig.4.12, corresponding to *Sample 5_BC_600*. Here, the pore is located very close to the outer surface of the specimen, and its dimensions are $\sim 62 \times 90 \mu\text{m}$. In some cases, around and inside the porosity, high concentration of some elements can be found. It is the case for *Sample 7_BC_600* (Fig.4.13): in Fig.4.13.4 some lighter spots are present, corresponding to high concentrations of *HfC* (identified using the *Energy-dispersive X-ray spectroscopy* analytical technique). It is the same for Fig.4.12.

In Fig.4.14 it is possible to observe three carbides on the crack surfaces (*Sample 10_BC_600*). The example shown in Fig.4.13 is interesting also because two crack initiation points are present (Fig.4.13.2, red marks). The biggest pore is the cause of the propagation of the crack. To have an example of failure due to oxidation, it is

Table 4.6: Cause of failure of bicrystal specimens tested at 980°C.

Sample	Cause of failure
1_BC_980	Oxidation
2_BC_980	Oxidation
3_BC_980	Oxidation
4_BC_980	Oxidation
5_BC_980	Oxidation
6_BC_980	Oxidation
7_BC_980	Oxidation
8_BC_980	Oxidation
9_BC_980	Not failed
10_BC_980	Pore
11_BC_980	Oxidation
12_BC_980	Oxidation

**Figure 4.12:** SEM characterization of the bicrystal *Sample 5_BC_600*, (600°C), adapted [2].

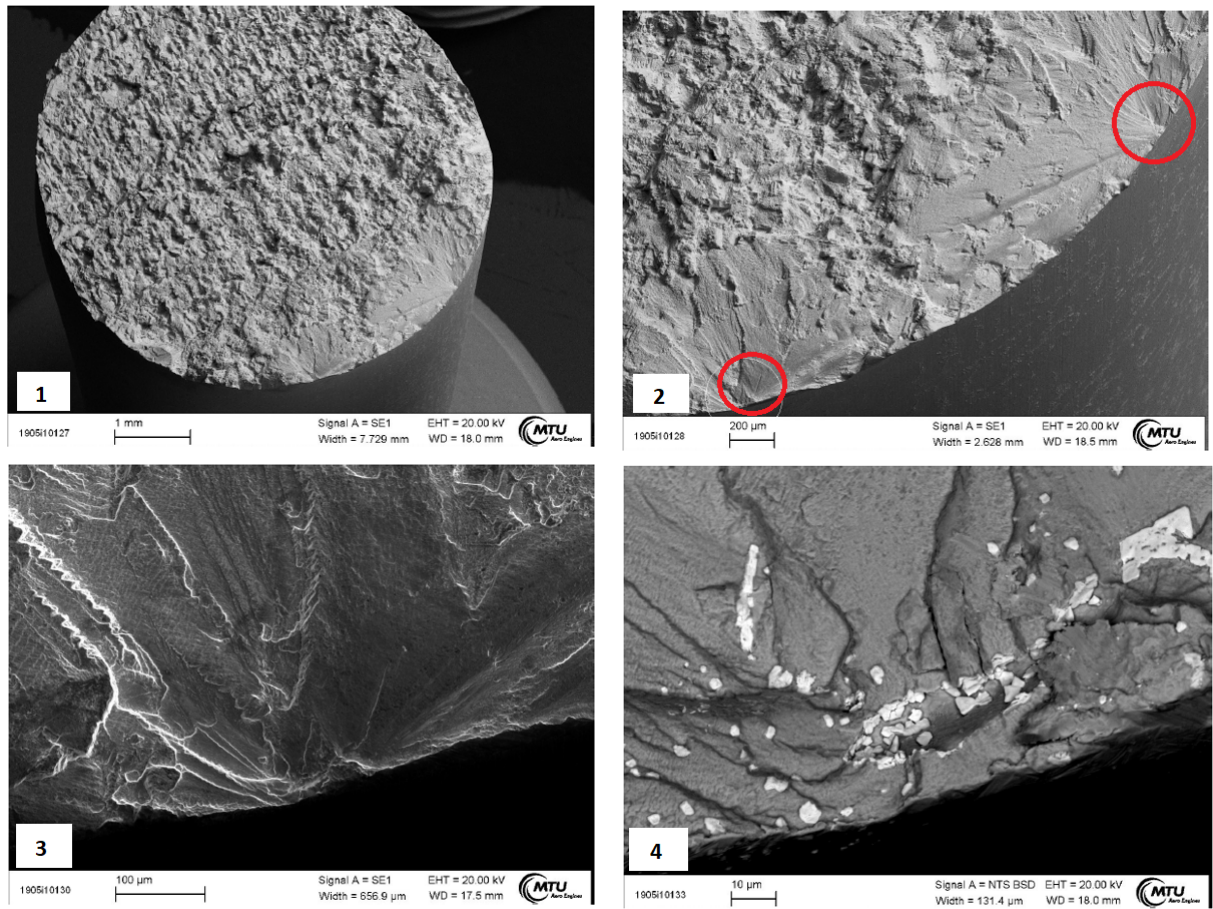


Figure 4.13: SEM characterization of the bicrystal *Sample 7_BC_600*, (600°C), adapted [2].

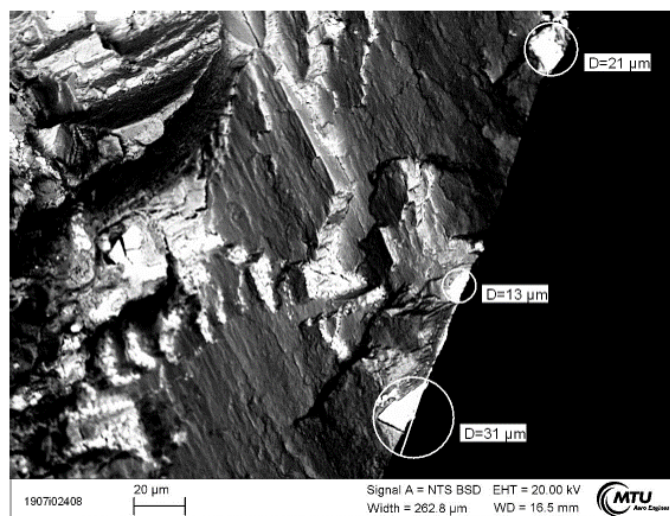


Figure 4.14: SEM characterization of the bicrystal *Sample 10_BC_600*, (600°C) [2].

possible to inspect *Sample 5_BC_980*, shown in Fig.4.15. When the failure is caused by oxidation, the oxidized area is well visible and its extension depends on the length of the crack. Moreover, as the temperature increases, the oxidized area increases as well. This is also visible in Fig.4.16. However, in rare situations, the surface is such that it is not possible to identify the crack initiation point, and consequently the cause of failure of the specimen. This is the case for *Sample 9_BC_600* (Fig.4.17).

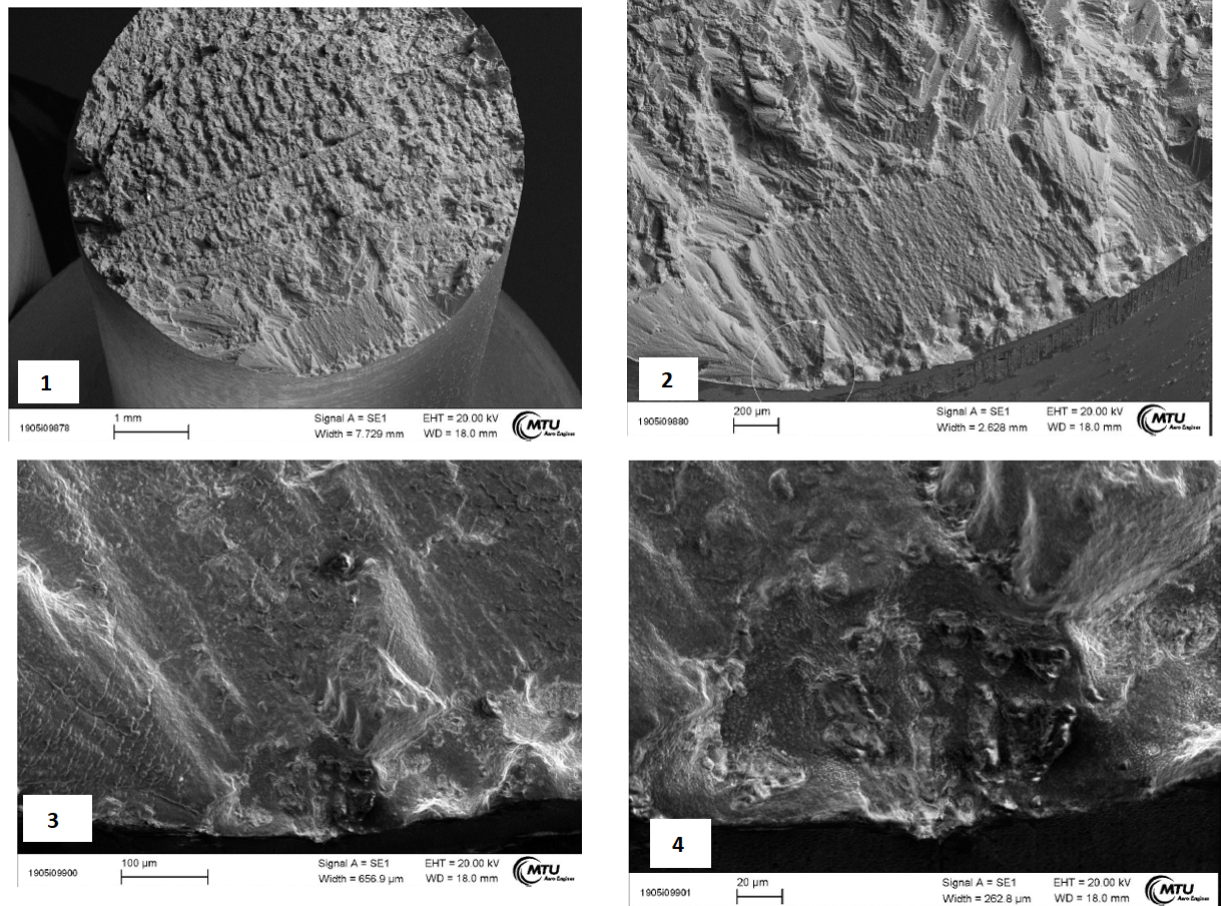


Figure 4.15: SEM characterization of the bicrystal *Sample 5_BC_980*, (980°C); adapted picture from [2].

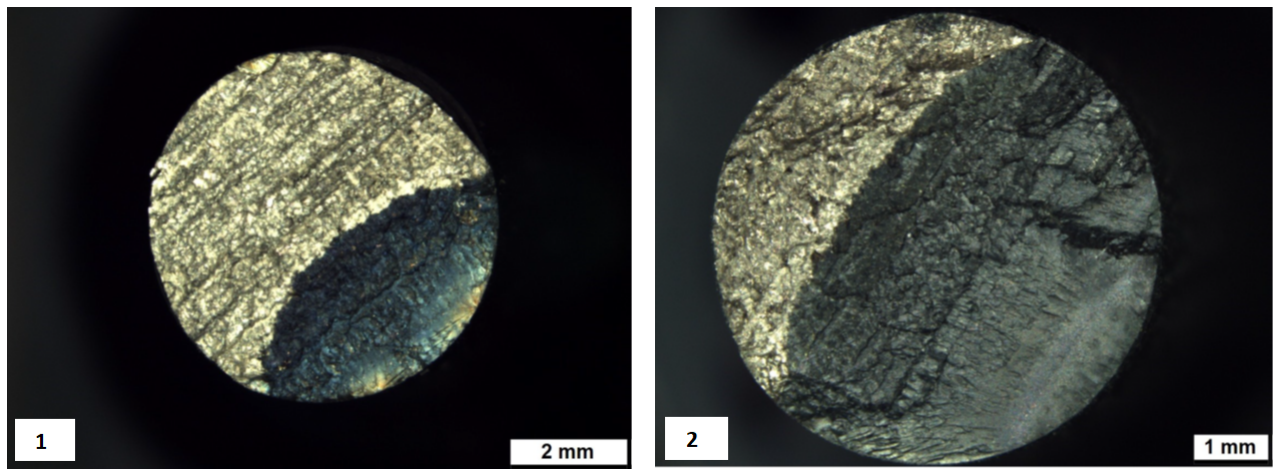


Figure 4.16: Comparison between two oxidized surface at 600°C (left) and 980°C (right); adapted picture from [2].

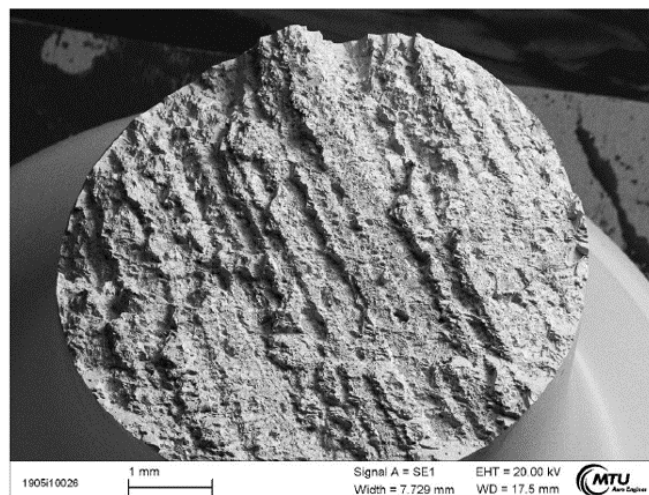


Figure 4.17: SEM characterization of the bicrystal *Sample 9_BC_980*, (980°C) [2].

4.4.2 EBSD

For a more detailed analysis, seven of the tested bicrystal specimens have been characterized with the EBSD technique. In order to do that, each single sample has been cut along the loading direction, and divided into two equal parts (Fig.4.18). The list of the analyzed specimens is reported in Tab.4.7. The values of the grain

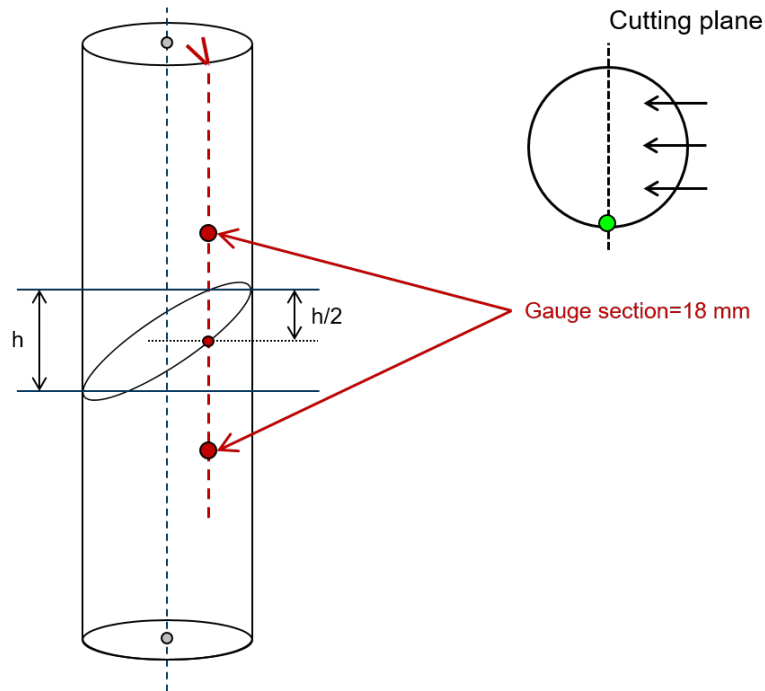


Figure 4.18: Sketch of sample and the reference cutting plane for EBSD measurements [2].

Table 4.7: Bicrystal specimens, EBSD analysis.

Sample	φ ($^{\circ}$)	α ($^{\circ}$)	T ($^{\circ}$ C)
1_BC_600	32	50	600
2_BC_600	32	50	600
3_BC_600	45	0	600
4_BC_600	45	0	600
1_BC_980	45	0	980
2_BC_980	45	0	980
3_BC_980	45	45	980

boundary inclination reported in Tab.4.7 is the one prescribed by the crystal seed when producing the plate.

In Tab.4.8 there are the Euler angles for each grain (defined as already discussed in *Paragraph 2.2*). The reference system in Fig.4.19 represents the position of the specimen in the microscope. Through the Euler angles (evaluated as already discussed in *Paragraph 2.2*), it is possible to calculate the real primary misorientation between the grains. This evaluation has been done using a *MATLAB* scrip, written by Ing. Markus Fried, that calculate the angle between the $\langle 001 \rangle$ vectors of the two grains. Another advantage coming from the EBSD is the possibility to find

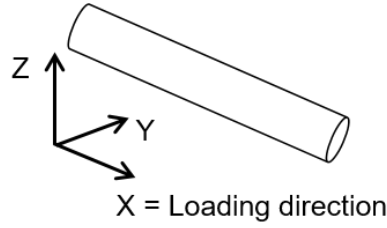


Figure 4.19: Reference system for the sample located inside the microscope.

Table 4.8: Euler angles determined with EBSD characterization.

Sample	Euler angles-Grain 1 ($^{\circ}$)	Euler angles-Grain 2 ($^{\circ}$)
1_BC_600	(177.7, 34.0, 3.9)	(188.7, 35.2, 28.1)
2_BC_600	(4.5, 44.3, 29.6)	(181.2, 47.1, 88.0)
3_BC_600	(22.6, 9.5, 17.5)	(345.5, 12.2, 6.5)
4_BC_600	(207.8, 5.0, 59.8)	(77.1, 3.5, 53.0)
1_BC_980	(174.4, 25.6, 4.2)	(103.8, 42.2, 60.4)
2_BC_980	(232.3, 2.9, 32.9)	(45.9, 5.3, 352.0)
3_BC_980	(297.6, 5.6, 93.4)	(0.4, 5.1, 88.9)

out the real grain boundary inclination. In Fig.4.20, for all the specimens, the micrographs corresponding to the results of the EBSD characterization are reported. In each micrograph, *Grain 1* and *Grain 2* are marked, respectively, and the same has been done for the grain boundary inclination. Having from the EBSD characterization the real values of α and φ , it is possible to compare them with the ones previously assumed (Tab.4.9). The values for φ are in a good agreement. Concerning α , there are more differences, in particular for $\alpha = 0^{\circ}$. Concerning the position of the crack initiation point, it is clear from Fig.4.20, that the failures occurs in the proximity of the grain boundary. In particular, the crack initiation point is in one of the corners of the grains, on the left or on the right side.

Table 4.9: Values of α and φ : EBSD VS Assumption.

Sample	α ($^{\circ}$)	α_{EBSD} ($^{\circ}$)	φ ($^{\circ}$)	φ_{EBSD} ($^{\circ}$)
1_BC_600	50	45	32	34
2_BC_600	50	50	32	32
3_BC_600	0	19	45	42
4_BC_600	0	16	45	43
1_BC_980	0	16	45	44
2_BC_980	0	0	45	43
3_BC_980	45	50	45	32

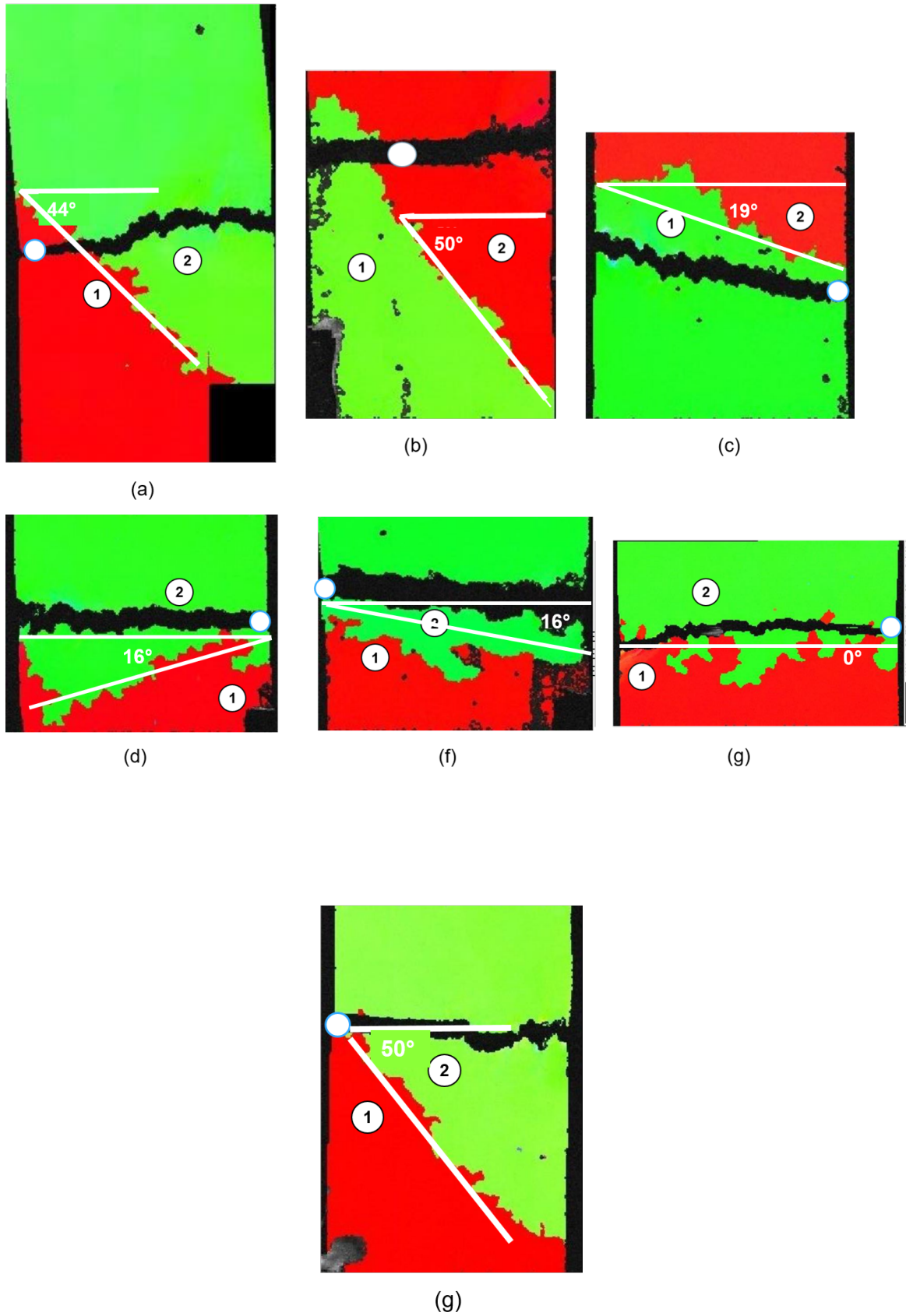


Figure 4.20: EBSD characterization for *Sample 1-7*, pictures (a)-(g) [2].

Chapter 5

Simulations

5.1 Introduction

The finite element modelling (FEM) technique is a numerical method for solving complex physical problems. It is used to reduce the number of experiments and optimize components in their design phase. FEM works by subdividing a 3D model into a certain number of smaller parts called *finite elements*. These elements have a defined shape. The number of elements is dependent on the *average element size*, a numerical value that determines the size of each of these elements. All the elements together constitute the *mesh* of the 3D model. The subdivision of a whole domain into simpler parts has several advantages [24]:

- Accurate representation of complex geometry
- Easy representation of the total solution of the simulation
- Capture of local effect

As much as the element size is reduced, an increase of:

- The accuracy of the analysis
- The time necessary for the calculation

is observed. The desired analysis is conducted on each finite element, considering all of them as having the same features. To this discretization of the component in elements, sets of equations are associated. The role of the FEM tool is to solve these equations, that describe the physical condition that has to be reproduced, and then give a final result. The result depends on the simulation that was launched, and corresponds to a distribution of a given physical parameter (for example displacement, stress, strain, temperature) over the entire sample.

5.2 The 3D model

The commercial software Hypermesh is a finite element pre-processor developed by the company *Altair Engineering Inc.*[25]. It is able to generate a Computer

Aided Design (CAD) geometry and then to create meshes in an automated manner. Firstly, a sample with the same geometry of the tested ones has been drawn. In Fig.4.3 the technical drawing of the tested sample is shown. Fig.5.1 shows the CAD



Figure 5.1: CAD geometry of the LCF specimen drawn with Hypermesh.

geometry of the 3D model having the same dimensions as reported in Fig.4.3. As already mentioned, Hypermesh is able to generate a mesh over the 3D model. This is what has been done as a second step using that tool. The final result is shown in Fig.5.2. The elements of the mesh have a tetrahedral shape. Their dimension has

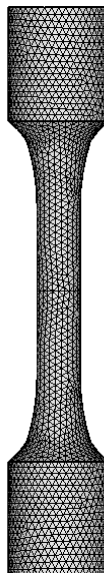


Figure 5.2: CAD geometry of the LCF specimen with the generated mesh.

been changed in the following steps, giving different values for the gauge length and the remaining part of the specimen.

In order to perform meaningful simulations, it is important to define the properties of the CAD model coherently with the ones of the real specimen. That means,

that also in the CAD geometry it is necessary to have two grains. This can be done separating the elements into two different groups called *sets*. All the elements belonging to the same set will have the same orthotropic material characteristics, and will therefore behave in the same way, Fig.5.3. The model is divided into two

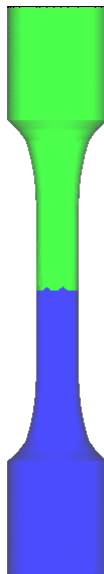


Figure 5.3: CAD geometry with the two different sets of elements.

sets, the green one, representing the upper grain, and the blue one, representing the lower grain. A stiffness tensor that corresponds to crystal orientation is assigned to each grain. This configuration correctly represents a bicrystal sample.

5.3 The script

The core of the simulations is the script, that reads an input file containing all the parameters needed for simulation and the model generated by Hypermesh. This script is written in *Linux shell* and *Python* [26] programming language by Ing. Frank Voese [2] and Dr.-Ing. Juergen Albiez. The script finally starts finite element analyses (FEA). Two different programs have been used.

CalculiX CrunchX and Abaqus FEA are software suits for finite element analysis. CalculiX is an open-source tool that has been developed by Ing.-Dr. Guido Dhondt and Ing. Klaus Wittig at MTU [27]. Abaqus has been produced by ABAQUS Inc., a company acquired by Dassault Systemes in 2015 [28] [29]. For the execution of the simulation both programs were used, preferring Abaqus for more complex simulations and therefore having a longer duration.

As already mentioned, the script contains all the parameters necessary to define the condition of the simulations. In particular, the input data are the following:

- Material properties depending on crystal orientation
- The primary misorientation between the two grains (φ): deviation from the loading direction

- The secondary misorientation between the two grains: rotation about the loading direction
- The grain boundary inclination (α)
- The maximum element size
- The temperature
- The applied load cycle (max/min nominal stress)

The misorientation and the grain boundary inclination are related to the crystallographic parameters of the materials. They define, respectively, the crystallographic mismatch and the grain boundary inclination of the bicrystal specimen.

For the reason mentioned before, the value of the element size plays an important role in quality of the simulation. With Hypermesh it is possible to generate a first mesh on the 3D model. However, the same accuracy is not needed everywhere in the specimen. The area of interest is the one located close to the grain boundary, which is the gauge section. For that reason, the script has been developed in order to be able to impose different values of the element size in the gauge area and in the the remaining part of the specimen.

The testing conditions have to be correctly reproduced, that is why the script is organized into two main calculation steps:

1. Tension
2. Compression

That means that for both the steps a specific load can be applied and also a specific temperature.

Another potentiality of the script used is the ability to define the properties of the material, considering it as purely elastic or plastic. For both the mentioned conditions, elastic and plastic, the structure of the script is the same. The only difference can be found in the way used to define the material properties, and consequently in the theory behind that. These models are briefly described in the following paragraphs.

5.3.1 Orthotropic and cubic linear elasticity model

The elastic model is based on the Hooke's law, that for anisotropic materials is written as

$$\sigma = C \cdot \epsilon \quad (5.1)$$

where σ is the *stress tensor*, ϵ is the *strain tensor* and C is the *elastic stiffness tensor*. Reporting all the terms of the tensors and considering the symmetry properties that characterize them, eq.5.1 can be written in the following way [30]:

$$\begin{bmatrix} \sigma_{11} \\ \sigma_{22} \\ \sigma_{33} \\ \sigma_{23} \\ \sigma_{31} \\ \sigma_{12} \end{bmatrix} = \begin{bmatrix} C_{11} & C_{12} & C_{13} & 0 & 0 & 0 \\ C_{12} & C_{22} & C_{23} & 0 & 0 & 0 \\ C_{13} & C_{23} & C_{33} & 0 & 0 & 0 \\ 0 & 0 & 0 & C_{44} & 0 & 0 \\ 0 & 0 & 0 & 0 & C_{55} & 0 \\ 0 & 0 & 0 & 0 & 0 & C_{66} \end{bmatrix} \cdot \begin{bmatrix} \epsilon_{11} \\ \epsilon_{22} \\ \epsilon_{33} \\ 2\epsilon_{23} \\ 2\epsilon_{31} \\ 2\epsilon_{12} \end{bmatrix} \quad (5.2)$$

Equivalent versions of eq. 5.1 and eq.5.2 are respectively, eq.5.3 and eq.5.4 [31]:

$$\epsilon = S \cdot \sigma \quad (5.3)$$

$$\begin{bmatrix} \epsilon_{11} \\ \epsilon_{22} \\ \epsilon_{33} \\ \gamma_{12} \\ \gamma_{13} \\ \gamma_{23} \end{bmatrix} = \begin{bmatrix} \frac{1}{E_1} & -\frac{\nu_{21}}{E_2} & -\frac{\nu_{31}}{E_3} & 0 & 0 & 0 \\ -\frac{\nu_{12}}{E_1} & \frac{1}{E_2} & -\frac{\nu_{32}}{E_3} & 0 & 0 & 0 \\ -\frac{\nu_{13}}{E_1} & -\frac{\nu_{23}}{E_2} & \frac{1}{E_3} & 0 & 0 & 0 \\ 0 & 0 & 0 & \frac{1}{G_{12}} & 0 & 0 \\ 0 & 0 & 0 & 0 & \frac{1}{G_{13}} & 0 \\ 0 & 0 & 0 & 0 & 0 & \frac{1}{G_{23}} \end{bmatrix} \cdot \begin{bmatrix} \sigma_{11} \\ \sigma_{22} \\ \sigma_{33} \\ \sigma_{12} \\ \sigma_{13} \\ \sigma_{23} \end{bmatrix} \quad (5.4)$$

where S is the inverse of tensor C , E_1 , E_2 , and E_3 are the three moduli, ν_{12} , ν_{13} , and ν_{23} are the Poisson's ratios and G_{12} , G_{13} , and G_{23} are the shear moduli associated with the material principal directions.

For a cubic lattice, the tensor S can be written as in eq.5.5:

$$S = \begin{bmatrix} S_{11} & S_{12} & S_{12} & 0 & 0 & 0 \\ S_{12} & S_{11} & S_{12} & 0 & 0 & 0 \\ S_{12} & S_{12} & S_{11} & 0 & 0 & 0 \\ 0 & 0 & 0 & S_{44} & 0 & 0 \\ 0 & 0 & 0 & 0 & S_{44} & 0 \\ 0 & 0 & 0 & 0 & 0 & S_{44} \end{bmatrix} \quad (5.5)$$

where S_{11} , S_{12} , and S_{44} are defined as in eq.5.6-5.8, for a rotational symmetry with respect to $\langle 100 \rangle$ - axis (90°), $\langle 111 \rangle$ - axis (120°) and $\langle 110 \rangle$ - axis (180°):

$$S_{11} = \frac{1}{E_{100}} \quad (5.6)$$

$$S_{12} = -\frac{\nu_{010,100}}{E_{100}} \quad (5.7)$$

$$S_{44} = -\frac{1}{G_{010,100}} \quad (5.8)$$

5.3.2 Crystal plasticity model

V. Kindrachuk and B. Fedelich generated a model able to describe the behavior of Nickel-based superalloy, predicting stresses during complex strain-time load histories, at moderate and high temperatures [32]. In particular, it can describe, with good accuracy, creep, cyclic straining and thermo-mechanical loading in a large range of temperatures [32]. According to that model, the stress tensor can be defined as

$$\sigma = C : (\epsilon - \epsilon^{in}) \quad (5.9)$$

where σ is the stress tensor, C is the elasticity tensor, ϵ is the total strain and ϵ^{in} is the inelastic strain tensor. This inelastic strain tensor is defined as the sum of the viscoplastic strain (ϵ^{vp}) and the plastic strain (ϵ^p), as in the eq 5.10.

$$\epsilon^{in} = \epsilon^{vp} + \epsilon^p \quad (5.10)$$

5.3.3 Conditions of simulations

The element size As already mentioned, the element size plays an important role in the accuracy of the calculations. This accuracy is inversely proportional to the element size: the one increases if the other one decreases. However, a low value of the element size produces also an increase, not negligible, in the time necessary to complete the calculation. In the analyzed specimen, just the gauge section is of interest: this is the region located in the proximity of the grain boundary, where the stress concentration is expected. Accordingly, two different values of the element size are used for the mesh of the sample: a fine one in the gauge length, and a coarse one in any other place. In order to have a faster computation and at the same time acceptable results, the value 2 has been chosen for the max element size in the coarse meshed region.

To decide the value of the element size to use for the gauge length, a sensitivity study was done. Three different specimens have been modelled under the conditions reported in Tab.5.1.

Table 5.1: Element size sensitivity study: testing conditions.

Sample	α (°)	ϕ (°)	T (°C)	σ_{max}	σ_{min}
1	0	45	980	334	-318
2	0	45	980	661	-214
3	45	45	980	243	-169

The values of the element sizes used for the study are reported in Tab.5.2. After

Table 5.2: Element size values.

Element size
0.15
0.2
0.25
0.3
0.35
0.4
0.45
0.85
1.2
2

each calculation, a stress distribution has been obtained. What has been analyzed is how the peak stress changes as a function of the element size. The results are shown in Fig.5.4 Here, one can observe, that reducing the element size, the value of the peak stress increases until a saturated peak stress is obtained. Starting from the value 0.45 until 0.15, this rise is progressively reduced and a plateau region is defined. That means, that the accuracy of the calculation does not increase continuously but reaches a maximum, when the curve has a convergent type trend. Based on that results, the element size of the gauge section used for all the calculations was decided to be 0.45. This value give at the same time reasonable accuracy and limited computational costs.

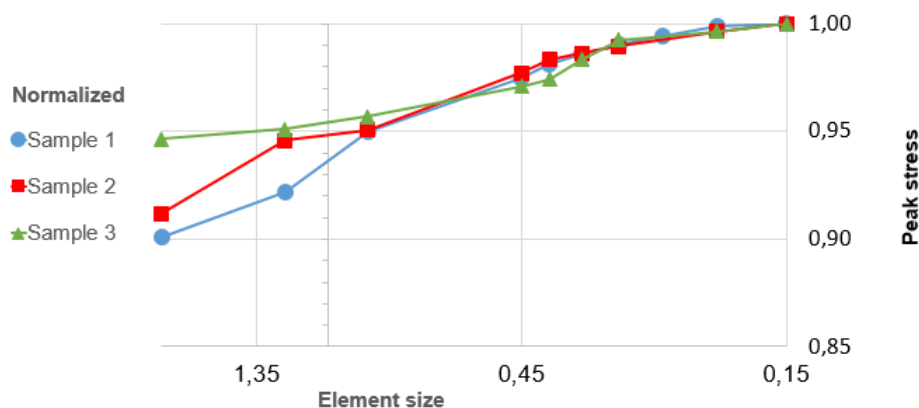


Figure 5.4: Normalized peak stress as a function of the element size.

Loading condition It is important to notice, that the simulations are conducted in stress controlled mode, even if the experiments are performed in strain controlled mode. We conclude this to be a minor issue because what has been observed from the experiments is, that in the strain controlled mode, after a few number of cycles the stress stops to increase and reaches a saturation value until the failure [2]. This behavior is not function of the temperature, see (Fig.5.5 and Fig.5.6). These results have been obtained after LCF tests conducted in strain con-

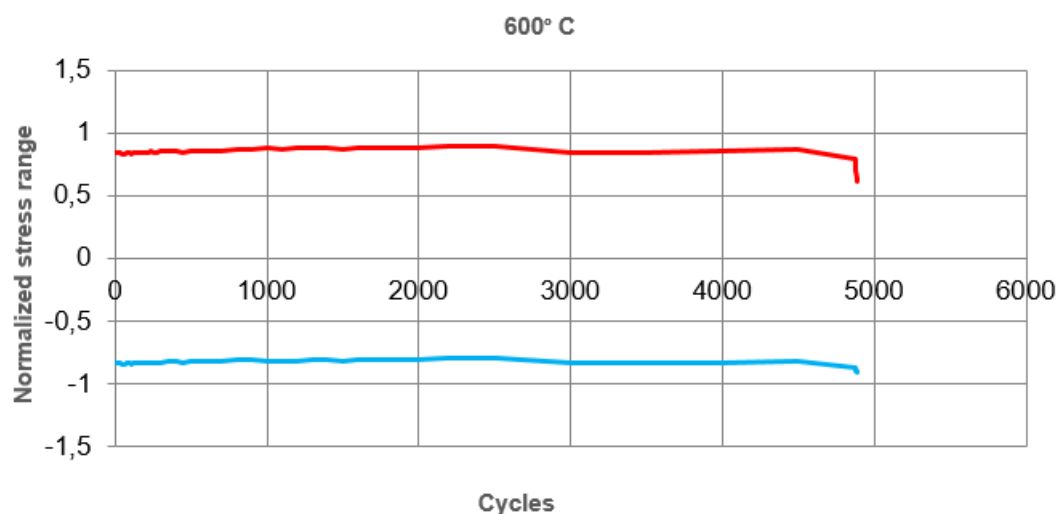


Figure 5.5: Normalized stress range as a function of the number of cycles at 600°C, strain controlled mode; adapted graph from [2].

trolled mode with a strain rate (%/s) of 0.3 and a triangular waveform [2]. After a preliminary phase of adjustment of the experimental set-up, the stress range reaches a steady state condition and remains constant until the end of the test, coinciding with the failure of the specimens. These results justify the procedure adopted for the simulations.

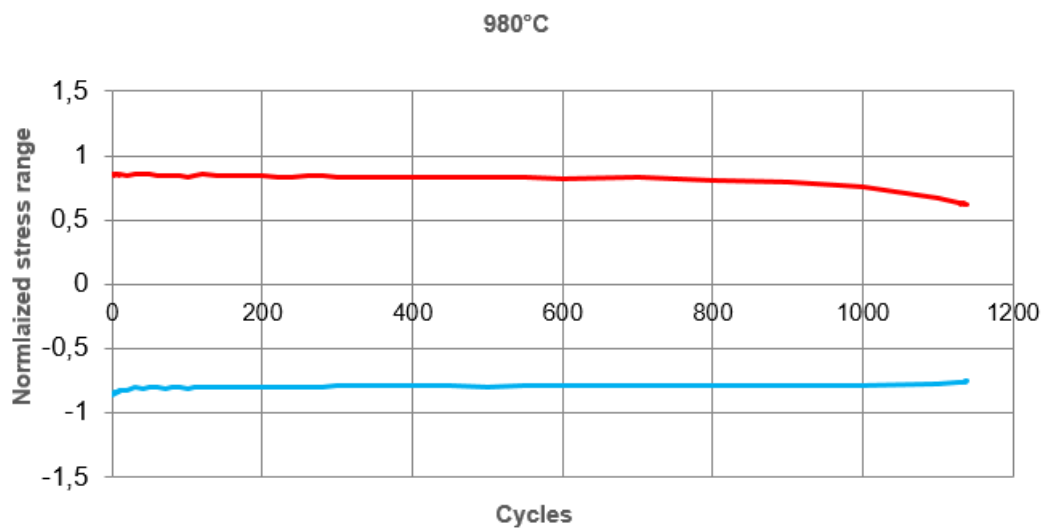


Figure 5.6: Normalized stress range as a function of the number of cycles at 980°C, strain controlled mode; adapted graph from [2].

Chapter 6

Discussion

In this chapter, grain boundary inclination, primary misorientation, and secondary misorientation are discussed. Then, a comparison between the experiments and calculations is done, to validate the model used.

Finally, a fatigue life prediction based on the results of the calculations is proposed.

6.1 Grain boundary and primary misorientation

The role of grain boundary inclination and primary misorientation is here described, distinguishing between the elastic and plastic model.

6.1.1 Elastic model

To evaluate the effect of the grain boundary inclination (α) and the primary misorientation (φ) on a bicrystal specimen, several simulations have been done. The attention has been focused on the dependency of the stress on these two parameters. Three *Series* of elastic simulations have been launched with the following values of temperature and load (σ_{nom}):

- *Series 1*: 600° C, \pm 600MPa
- *Series 2*: 600° C, \pm 300MPa
- *Series 3*: 980° C, \pm 250MPa

The values of the temperature used are the same as in the experiments, 600°C and 980°C. Also 600MPa is a typical load deduced from the experiments.

For 600°C, two different loading conditions have been considered to observe if the amplitude of the load has relevant impact on the final results. The primary misorientations evaluated are the same as in the real specimens: 16°, 32°, and 45°. A large range of angle for the grain boundary inclination has been used: it varies from -70° to 70° taking each value every 5°. An overview of the simulations described so far is given in Tab.6.1. The results are shown in Fig.6.2. On the X-axis the grain boundary inclination values are shown. The Y-axis reflects the stress concentration factor f_σ . This coefficient is defined as the ratio between the peak stress, obtained

Table 6.1: List of the elastic simulations and their configuration.

Series	T (°)	σ_{nom} [MPa]	φ (°)	α (°)
1	600	± 600	{16, 32, 45}	[-70,70]
2	600	± 300	{16, 32, 45}	[-70,70]
3	980	± 250	{16, 32, 45}	[-70,70]

as a result of the simulations, and the nominal stress, the one imposed to run the calculations (eq.6.1).

$$f_{\sigma} = \frac{\sigma_{peak}}{\sigma_{nom}} \quad (6.1)$$

In the plots, the yield strength has been introduced as a guideline for the study of the results. The value used for that parameter comes from MTU internal database [2]. Fig.6.1 (a) displays the results related to *Series 1*. The data show, that for $\varphi = 16^{\circ}$ and for values of α in the range $[-70^{\circ}, 50^{\circ}]$, f_{σ} is not affected by significant variations. In fact, f_{σ} takes values between 1.2 and 1.6.

For $\varphi = 32^{\circ}$, f_{σ} is more sensitive to changes in the grain boundary inclination and is in the range from 1.4 to 2.4.

The shape of the curve changes considerably when $\varphi = 45^{\circ}$: for this primary misorientation, the value of f_{σ} is almost constant for α in the range $[-30^{\circ}, +30^{\circ}]$, and it is symmetric compared to $\alpha = 0^{\circ}$. This symmetry is absent for the other two misorientations.

For all the misorientations considered, when $\alpha > 50^{\circ}$, the stress concentration factor overcame the yield strength. That means, that for high values of the grain boundary inclination, local plasticity has to be taken into account. In fact, all the results shown so far, have been obtained using the elastic model, that considers the material as purely elastic.

In Fig.6.1 (a), (b), (c) one notes that the applied load and the temperature does not change the shape of the curves. Accordingly, what has been concluded for *Series 1* is valid also for *Series 2* and *Series 3*.

An additional observation can be done concerning f_{σ} . σ_{peak} , that represents the maximum stress measured in the sample after the simulation.

An alternative to calculate the maximum principal stress is proposed by the *Weakest link theory*, that considers the specimens having a notch (more information in *Appendix A.2*). In this way, a new parameter called f_l can be introduced. This coefficient f_l is equivalent to f_{σ} and is defined as below (eq.6.2):

$$f_l = \frac{\sigma_{wl}}{\sigma_{nom}} \quad (6.2)$$

where σ_{wl} is the maximum stress reached in the specimens calculated using the weakest link theory. In Fig.6.2, f_l is plotted against α for all the series. Comparing Fig.6.2 with Fig.6.1, it is observed, that the shape of the curves does not change. That means that the observations that have been done for f_{σ} are valid also for f_l . Instead, there is a difference concerning the range of values for f_l : for equal α and φ , f_l is lower than f_{σ} . That happens because the maximum stress calculated with the weakest link theory is lower than the maximum principal stress. Moreover, f_l curves are smoother than f_{σ} ones.

For a more detailed analysis, it can be interesting to look at the stress distribution in the samples, and how it is modified by changing the misorientation and the grain

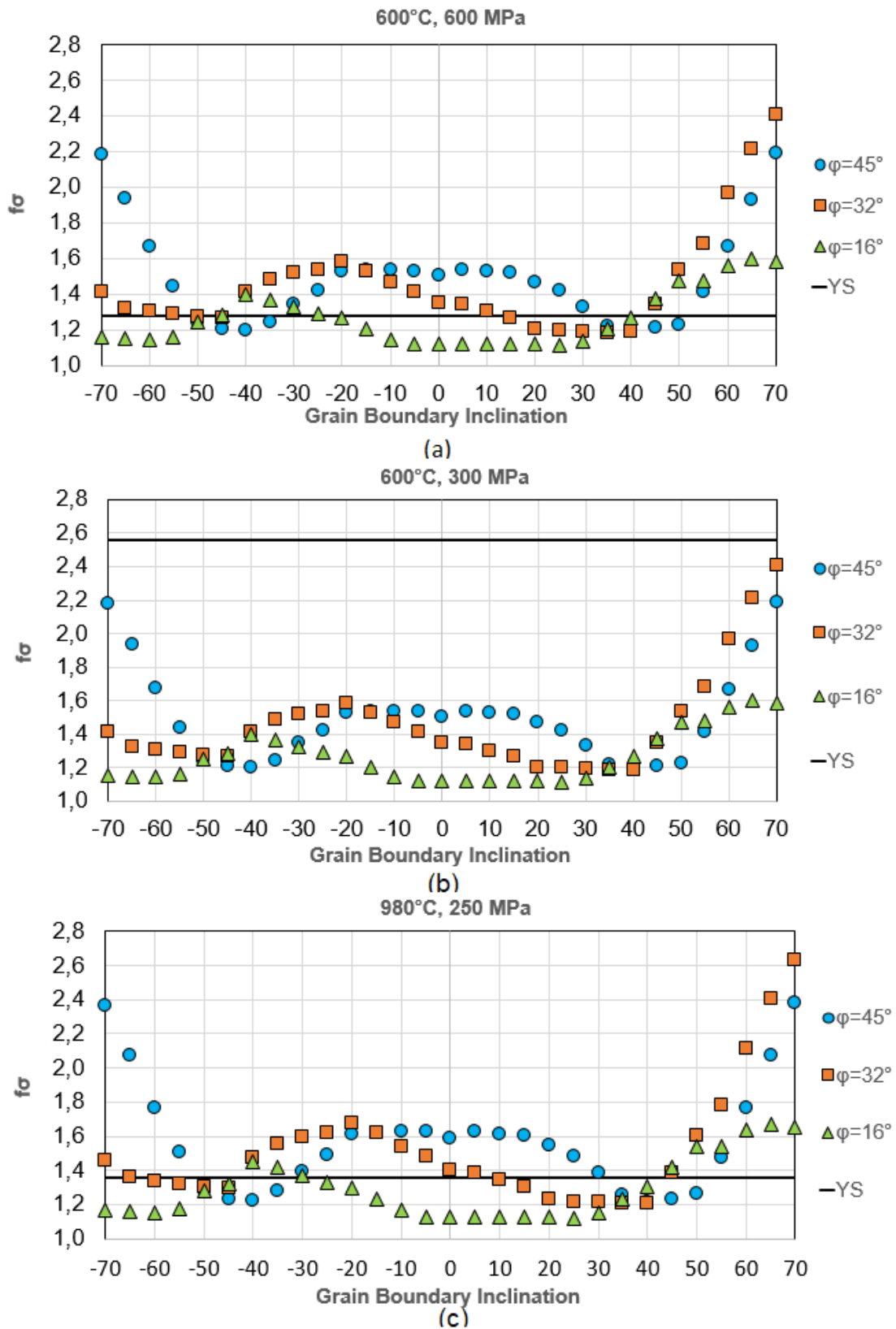


Figure 6.1: Stress concentration factor against grain boundary inclination (α) for *Series 1* (a), *Series 2* (b), and *Series 3* (c).

boundary inclination. In Fig 6.3 the stress distributions for *Series 1* are displayed. Looking at the stress distribution for $\varphi = 16^\circ$, the grain boundary inclination has

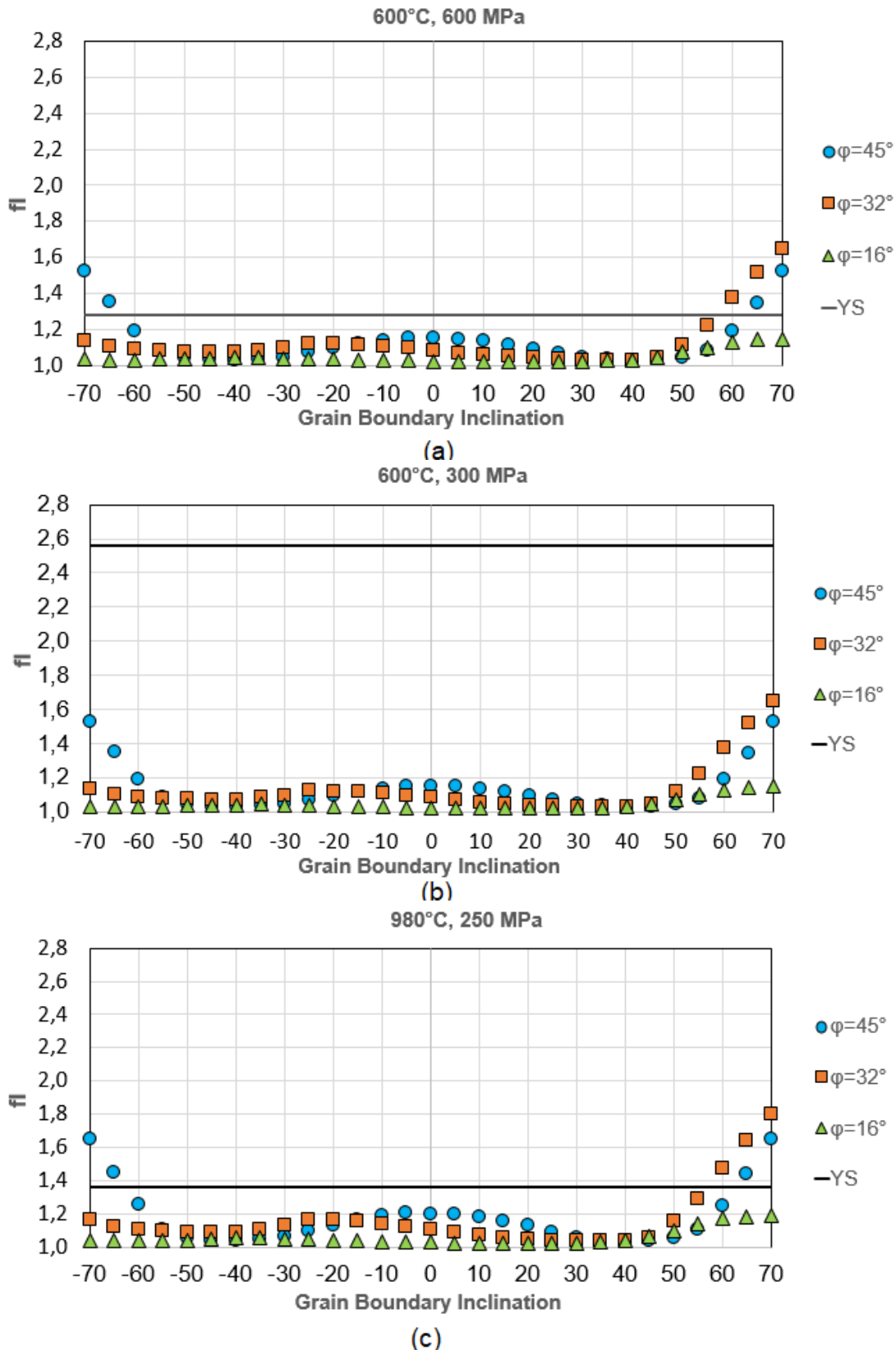
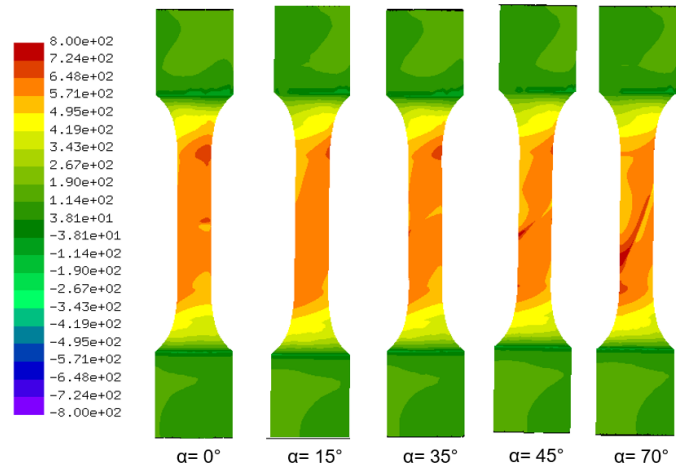
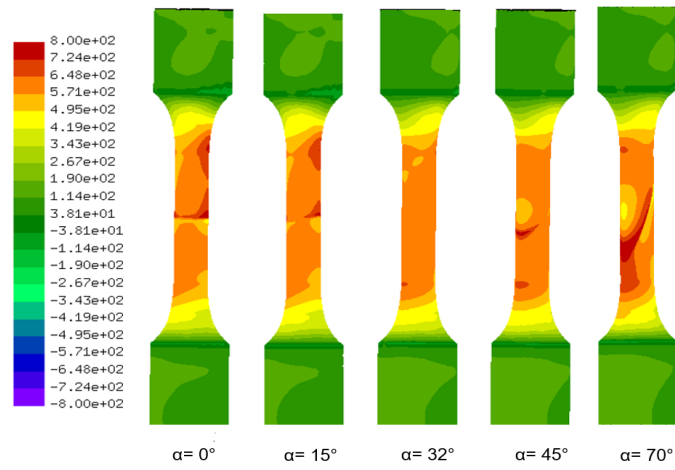


Figure 6.2: Stress concentration factor against grain boundary inclination (α) for *Series 1* (a), *Series 2* (b), and *Series 3* (c).

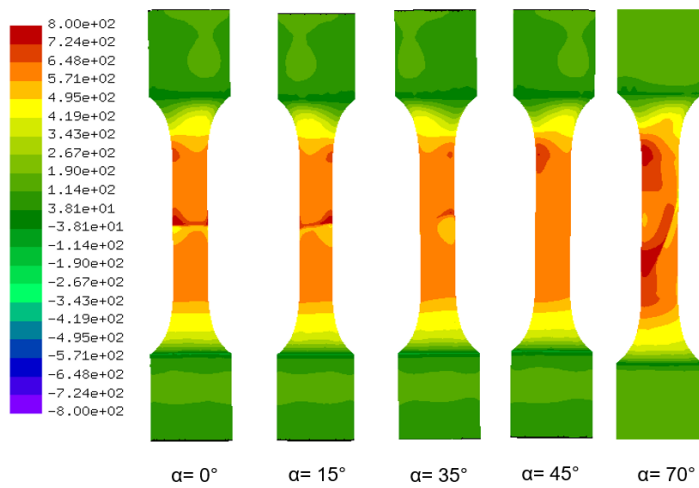
effect on stress distribution beginning from $\alpha = 45^\circ$. In fact, for values lower than the last mentioned one ($\alpha = 45^\circ$), stress concentrations are not visible on the samples.



(a)



(b)



(c)

Figure 6.3: Stress distribution as a function of α , for $\varphi = 16^\circ$ (a), $\varphi = 32^\circ$ (b), and $\varphi = 45^\circ$ (c).

For $\varphi = 32^\circ$, an increase in the stress is observed already since $\alpha = 0^\circ$. The same observation is valid for $\varphi = 45^\circ$. Moreover, for each misorientation, the highest stress is obtained for $\alpha = 70^\circ$. The stress concentration is located exactly in the proximity of the grain boundary. This result is in perfect agreement with the observations in the EBSD micrographs: the stress distributions in Fig.6.3 shown that the highest stresses are reached at the outer edges on the grain boundary, exactly where the specimens failed after the experiments. A smaller area with a considerable high stress is visible also outside the gauge section, at the upper side of the specimen. This stress concentration is due to the shape of the specimen, and in particular to the radius of the sample in that point. Moreover, the material is anisotropic, and in accordance with what is described in eq.5.4, some stresses perpendicular to the loading direction, are present.

6.1.2 Plastic model

Since plastic deformation phenomena have been observed for high grain boundary inclinations, the same study described in the paragraph above has been done with the plastic model. In this case, two series of simulations have been executed:

- *Series 1*: 600°C , $\pm 600\text{MPa}$
- *Series 2*: 980°C , $\pm 250\text{MPa}$.

The configuration equivalent to *Series 2* ($600^\circ\text{C} \pm 300\text{MPa}$), performed with the elastic model, has been neglected since, as already discussed, the applied load does not affect the shape of the curve (Fig.6.1 (a), (b) and also Fig.6.2 (a), (b)), and so the final result.

In this study, α takes just a selected number of values. The misorientations considered are still 16° , 32° , and 45° . Since the results obtained using the weakest link theory give a more accurate description for LCF and HCF in Nickelbase cast alloy [30], only the f_l factor is reported here. An overview of the simulations is given in Tab.6.2.

In this case, the results compare in the same graph elastic and plastic data, but just distinguish between the three different misorientations (Fig.6.4). The misorientation of 16° shows a perfect agreement between the elastic and the plastic model. Moreover, f_l does not take values above the yield strength. Almost the same can be said for $\varphi = 32^\circ$, excepted that a divergence between the elastic and plastic results take place when $\alpha > 50^\circ$. In case of $\varphi = 45^\circ$, there is still a symmetry for $\alpha = 0^\circ$ that is not observed with 16° and 32° . The f_l factor overcomes the yield strength for $\alpha > 50^\circ$ and $\alpha < -50^\circ$, and in the same ranges, differences between the elastic and plastic calculation are present.

In particular, f_l reaches lower values with the plastic model (this is due to the way the properties of the material are defined: see *Paragraph 5.3.1* and *Paragraph 5.3.2*). This is due to the plastic deformation phenomena, which occur as a result of the high inclination of the grain boundaries. At 980°C , the explanation is different: considering plasticity, at high temperature creep deformation is active, and this causes a relaxation of the stresses. The results do not change with a temperature of 980°C (Fig. 6.5). In this case, the divergence for $\alpha > 50^\circ$ can be explained as a consequence of creep and stress relaxation.

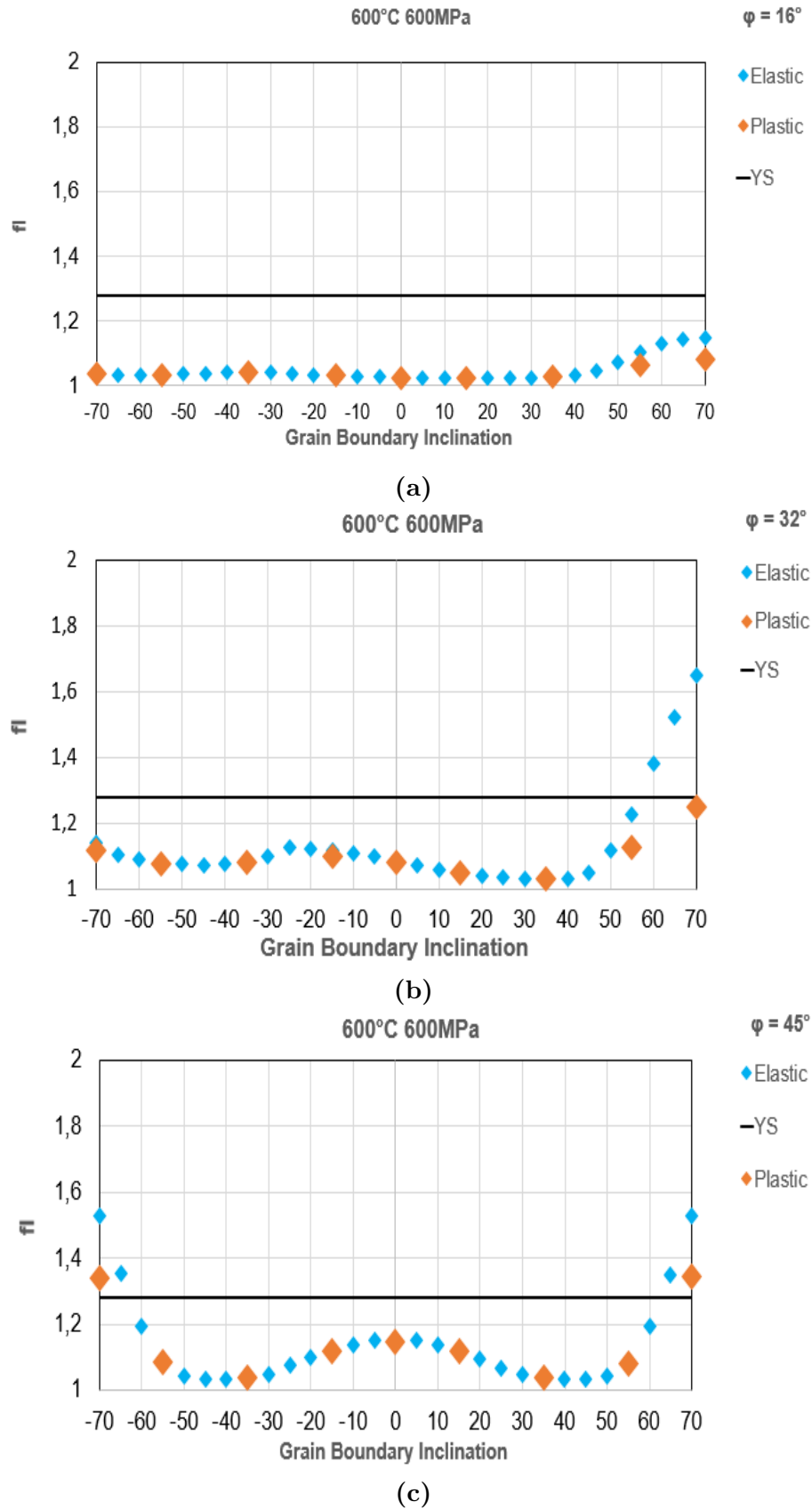


Figure 6.4: Stress concentration factor as a function of α at 600°C, for $\varphi = 16^\circ$ (a), $\varphi = 32^\circ$ (b), and $\varphi = 45^\circ$ (c).

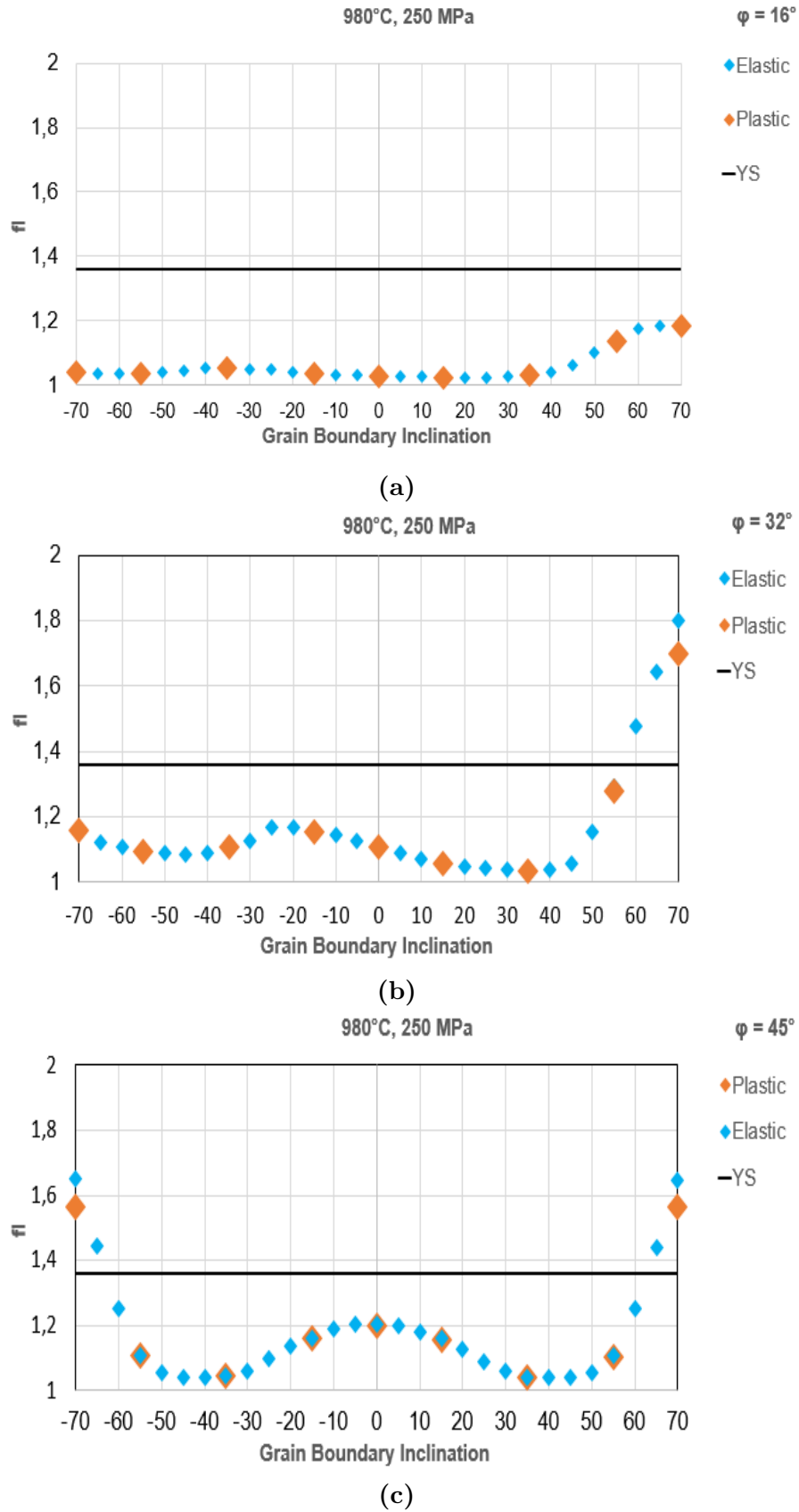


Figure 6.5: Stress concentration factor as a function of α at 980°C, for $\varphi = 16^\circ$ (a), $\varphi = 32^\circ$ (b), and $\varphi = 45^\circ$ (c).

Table 6.2: List of the elastic simulations executed and their configuration.

Series	T (°)	σ_{nom} [MPa]	ϕ (°)	α (°)
1	600	± 600	{16, 32, 45}	{-70, -55, -35, -15, 0 15, 35, 55, 70}
2	980	± 250	{16, 32, 45}	{-70, -55, -35, -15, 0 15, 35, 55, 70}

6.2 Secondary misorientation

The effect of another parameter has been considered. Until now, just the role of the primary misorientation has been considered. However, the secondary misorientation can still assume any values. For that reason, a sensitivity study has been done also on that parameter using the plastic model. The conditions imposed for the simulations are listed in Tab.6.3 and Tab.6.4. In Fig.6.6, one can see the results of these simulations. For a primary misorientation $\varphi = 16^\circ$, the secondary misorientation does not have an effect on the stress reached by the sample after the simulation. A similar argumentation can be done for $\varphi = 32^\circ$, where the stress increases for a secondary misorientation of 45° but not in a relevant way. The situation is quite different for $\varphi = 45^\circ$. In this case, when the secondary misorientation is equal to 45° , the stress increases consistently, and then it begins to diminish.

Varying the temperature, the shape of the curves does not change its trend. The differences in the normalized values of the stress σ are due to the fact that the samples have been tested using different values of σ_{nom} .

Table 6.3: Sensibility study for the secondary misorientation at 600°C .

Sample	α (°)	φ (°)	Secondary misorientation (°)	σ_{nom} [MPa]
1	0	16	0, 15, 30, 45	533
2	50	32	0, 15, 30, 45	603
3	0	45	0, 15, 30, 45	630

In Fig.6.6, one can see the results of these simulations. For a primary misorientation $\varphi = 16^\circ$, the secondary misorientation does not have an effect on the stress reached by the sample after the simulation. A similar argumentation can be done for $\varphi = 32^\circ$, where the stress increases for a secondary misorientation of 45° but not in a relevant way. Different is the situation for $\varphi = 45^\circ$. In this case, when the secondary misorientation is equal to 45° , the stress increases consistently, and then it begins to diminish.

Table 6.4: Sensibility study for the secondary misorientation at 980°C .

Sample	α (°)	φ (°)	Secondary misorientation (°)	σ_{nom} [MPa]
1	45	16	0, 15, 30, 45	286
2	45	32	0, 15, 30, 45	260
3	0	45	0, 15, 30, 45	243

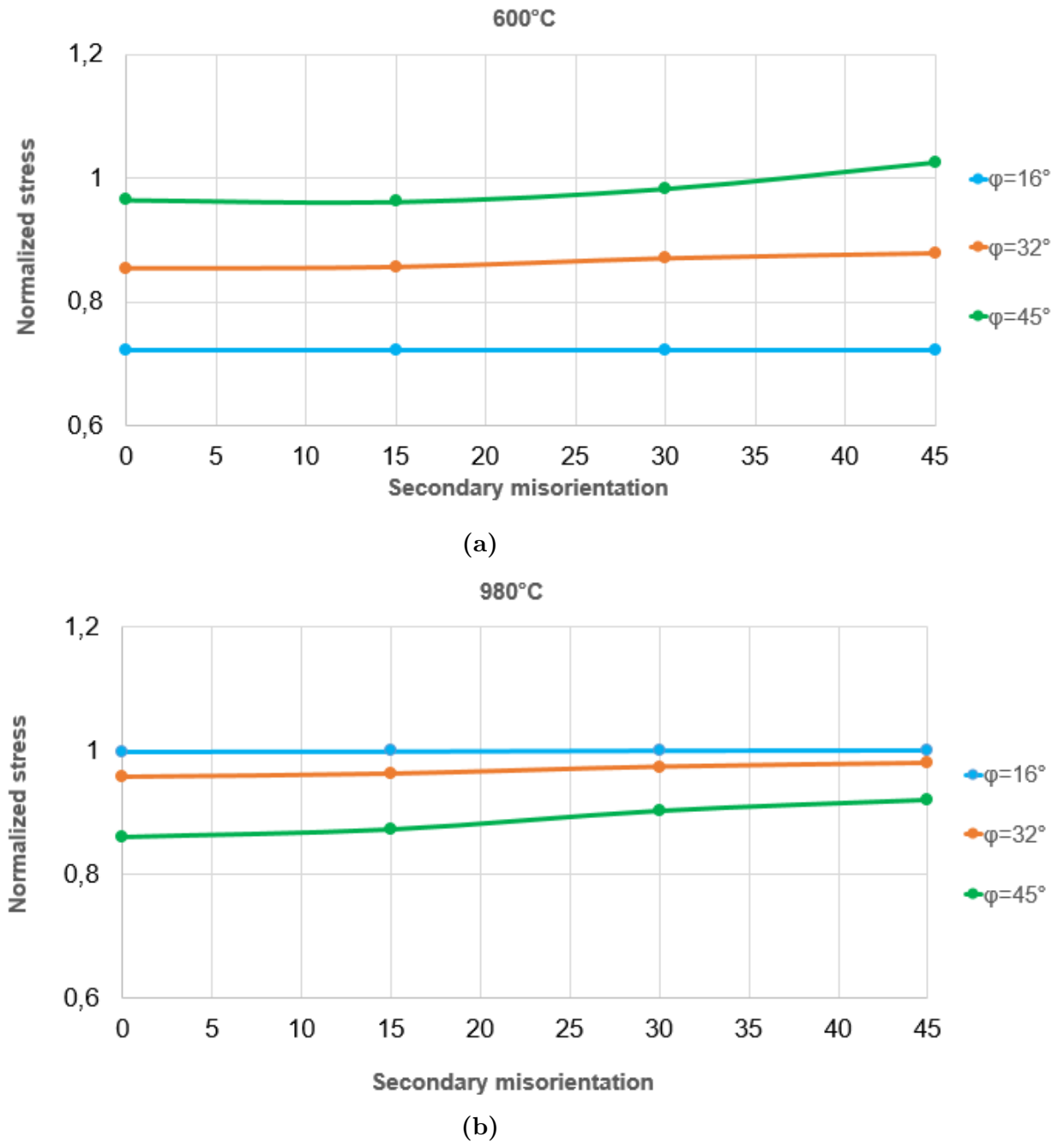


Figure 6.6: Sensibility study for secondary misorientation at 600°C (a), 980°C (b).

6.3 Comparison between experiments and simulations

The information collected so far can be used to validate the model used for the simulations. To be able to do that, the results obtained by the experiments have to be compared with the ones coming from the simulations executed in same conditions.

From the sensitivity study conducted for the grain boundary inclination and for the primary misorientation, it is possible to define a maximum and minimum value, both for f_σ and f_l . These values are shown in Tab6.5 for 600°C and ± 600 MPa (*Series 1*), using the plastic model. They have been used to define two scatter bands. In Fig.6.7, it is possible to see the curve representing the single crystal specimens, the curve for the bicrystals, and the scatter band for f_σ and f_l for 600°C. For brevity, just this temperature has been represented. As already discussed, there are no differences in the results changing the temperatures, excepted for the absolute values of the variables considered. Analyzing the graph, some conclusions can be

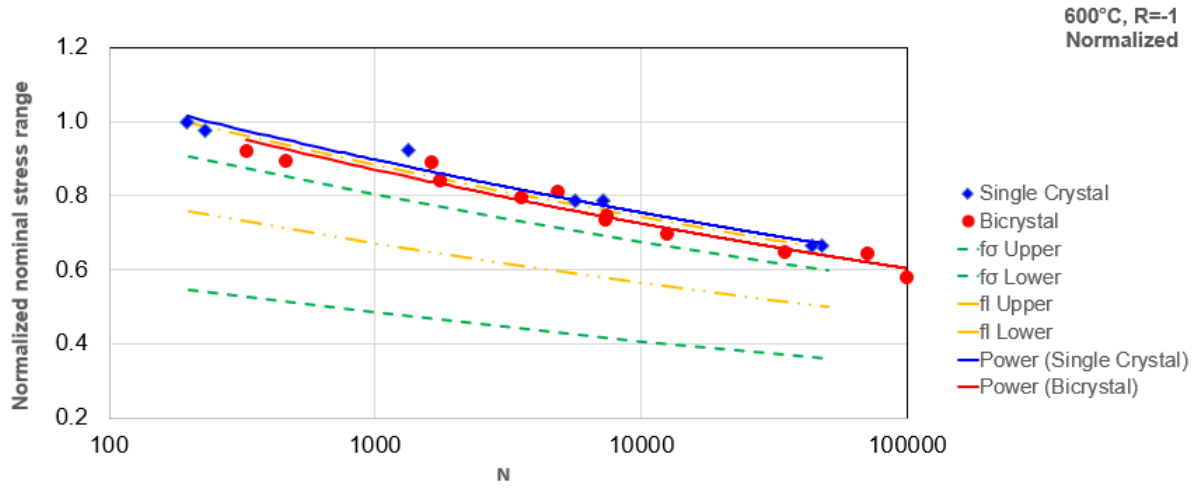


Figure 6.7: Comparison between experiments and simulations for 600°C.

drawn. The blue line represents the average line for the single crystal specimens. The two green dashed lines define the scatter band coming from f_σ whereas the two yellow dashed lines represent the scatter band for f_l .

As a first observation, the f_σ scatter band is below the one of f_l , that is closer to the single crystal points. This means that, as already discussed, the weakest link theory results are closer to the experiments. In fact, the red line, corresponding to the average curve for the bicrystals, is located exactly on the upper limit of this scatter band.

For what observed, it is possible to conclude that the plastic model, combined with the weakest link theory, gives as outputs of the calculations, stress values that are in closest agreement with the experiments.

Table 6.5: Maximum and minimum values of f_σ and f_l .

	MAX	MIN
f_σ	1.86	1.12
f_l	1.34	1.02

6.4 Life prediction

A life prediction of the tested specimens, based on the simulations, is proposed here. In fact, one of the outputs produced by the script is the number of cycles to failures.

The number of cycles predicted by the model have been compared with the ones obtained from the experiments (Fig.6.8). In the graph, two series are shown: one for the number of cycles obtained with the peaks stress theory, and the other one for the number of cycles obtained with the Weakest link theory. Points are expected to be in the scatter band depicted in the green in the plot. To define the amplitude of this scatter band, a value of 3 has been used, since considered typical for fatigue life prediction [2].

Looking at the data it possible to assert, that the Weakest link theory gives results that are in closer agreement with the experiments, represented by the grey line. In fact, the most of the blue points are located inside this scatter band. Concerning the red points, corresponding to the results of the peak stress theory, the most of them are outside the range defined in green. Nevertheless, this is still an acceptable result since it leads to a conservative life prediction. As already

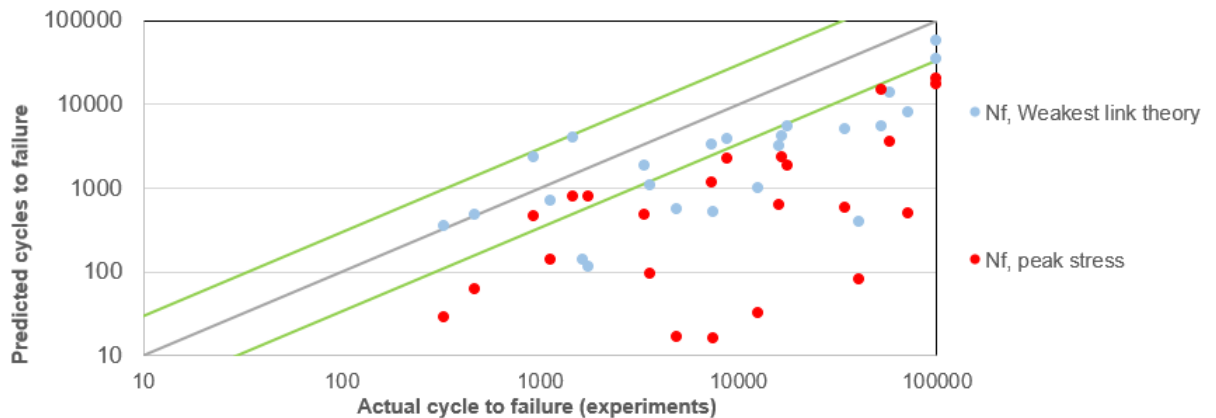


Figure 6.8: Life prediction: comparison between experiments and plastic simulations (logarithmic scale).

mentioned in *Chapter 4: Experiments*, seven specimens have been characterized with the EBSD technique to precisely calculate the primary misorientation. For this reason, the Euler angles of these seven specimens (Tab.4.8) have been used, instead of the exact numerical angle, to define the primary misorientation. The results present in Fig.6.9 are referred to the plastic model. It is interesting to compare, for this selected seven specimens, the two different life predictions described so far: the one based on the conventional script with the one that uses the Euler angles. This comparison is represented graphically in Fig.6.10. The results show that the script that uses as an input data the Euler angles, can guarantee a life prediction more accurate than the traditional model. Moreover, it is possible to assert, that the primary misorientation has clearly an effect on the life of the components, and not only on the stress distribution or concentration.

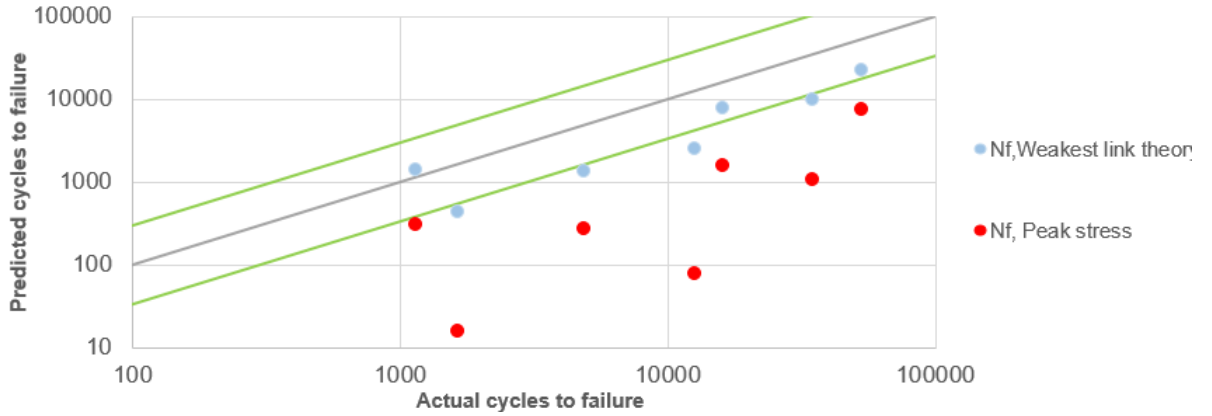


Figure 6.9: Life prediction: comparison between experiments and plastic simulations with Euler angles (logarithmic scale).

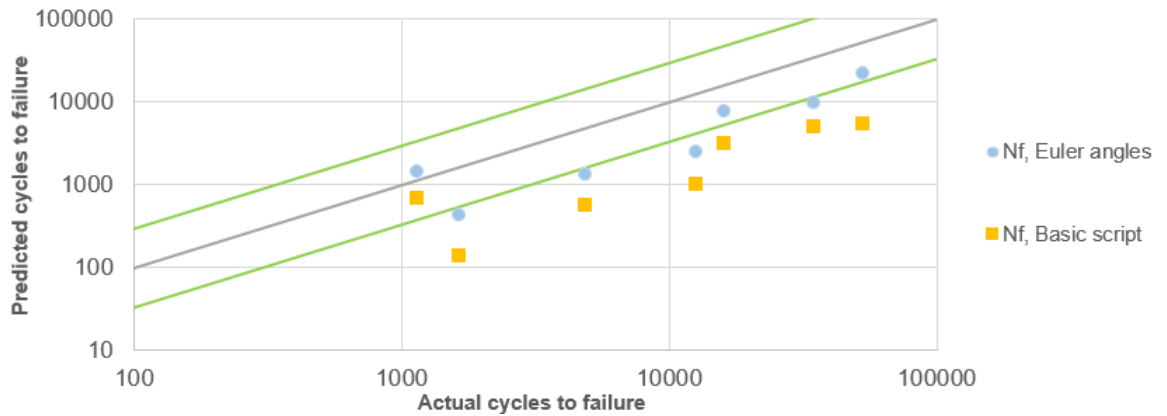


Figure 6.10: Life prediction: comparison between the conventional script (basic script) and the one with the Euler angles (logarithmic scale).

Chapter 7

Conclusion

The role of the grain boundary inclination and the primary misorientation on fatigue has been analyzed in detail, using different tools and methods.

Initially, the attention was paid to the alloy and its characteristics. The peculiar composition of alloy MAR M 247 made possible to go through a process of directional solidification, and hence to produce the bicrystal specimen necessary for the experiments.

The samples have been tested under low cycle fatigue at two different temperatures, 600°C and 980°C. The evaluation of the results has been performed by comparing the bicrystals with single crystal specimens tested under equivalent conditions. As a major outcome it could be stated, that the bicrystals have a behavior comparable to that of single crystals for both temperatures. Concerning the number of cycles to failure, they fall within the same range for both the types of specimens, thus also being totally comparable.

The SEM and EBSD characterizations have been helpful to understand that the testing conditions have a role in the cause of failure. In fact, at 600°C the most of the specimens failed because of pores. Conversely, at 980°C oxidation affects the life of the specimens, leading to failure. The crack initiation points analyzed are located close the grain boundary, in agreement with simulations. The grains boundary itself remained intact.

Correlating the experiments with FEM simulations, the quality and the amount of information has been increased. The FEM analysis made possible to clearly highlight how much the grain boundary inclination and the primary misorientation are important to define materials fatigue properties. A primary misorientation of 16° plays a less decisive role than 45° in inducing a stress concentration in the components. If the grain boundary inclination reaches values beyond 50° the description of the materials behavior utilizing the elastic model does not lead to satisfactory results anymore. In fact, in these cases the stress concentration results in a value greater than the yield strength of the alloy. That means, that for low values of the grain boundary inclination, the elastic model gives results that well describes the real components behavior. However, if this angle is higher than 50°, it is necessary to switch to the model which included plastic deformation.

The secondary misorientation has a relevant effect just on a primary misorientation of 45°: for a value of 45°, the stress in the specimens reaches a maximum.

Through a comparison between the experimental data and the results of the simulations, performed in a way equivalent to the tests, a validation of the used FE

model has been obtained. In greater detail, the Weakest link theory has proved to guarantee the most accurate materials description.

A major outcome from the fatigue life prediction is, that the model used for the simulations is able to produce an estimation of the life of the specimens that is highly conservative if compared to the effective number of cycles of the same specimens. A closer agreement between the experiments and the calculations has been observed when the crystallographic properties of the specimens are given in terms of Euler angles.

With all the information collected so far, the script represents a useful tool that can be employed for several applications. Firstly, it allows to establish if a material has the necessary features to be placed in use. Furthermore, due to its conservative behavior, the script enables to make a fatigue assessment as reliable as possible.

Although the results obtained up to this point are already satisfactory and useful for extending the knowledge concerning the fatigue behavior of materials, there are numerous improvements that can be achieved. The bicrystal specimen used for the experiments and for the simulations is an initial prototype, that hopefully, will be substituted by a material with columnar grains. That means that also the CAD geometry has to reproduce the columnar structure. As consequence, it can happen than grain boundaries with different inclinations will be close to each other. Their interaction, and the effect that this can have on the properties of the material, is something that would be reasonable to study. Furthermore, it is important to remember that the analyzed specimens have not been coated as is the case with real components. This is an aspect that cannot be neglected: coatings, and eventually coatings cracks, may have a huge impact on fatigue life. As a consequence, one of next goal to achieve in this study is the execution of experiments with coated materials, and an implementation of the script to consider the presence of these coatings in the simulations. However, then it is suppressed oxidation as a possible failure mechanism because of the presence of the coating.

The sensitivity study performed in secondary misorientation is still on its preliminary phase and needs to be developed further. Furthermore, until now just the LCF regime has been taken into account. Differences can be observed switching to the HCF or even UHCF regimes.

Appendix A

Appendix

A.1 The weakest-link theory

The first concepts of the weakest link theory have been proposed in 1939 by W. Weibull, in order to give a description of the tensile fracture of brittle solids [33]. In the context of these theory, it is assumed that the fatigue failure causing initial defects are spatially uniform distributed. The probability of failure is than only dependent on the individual size of the critical location - i.e. its volume V [30]. This probability is defined like in eq. A.1

$$dP = \left(\frac{\sigma}{\sigma_0}\right)^m \frac{1}{v_0} dV \quad (\text{A.1})$$

For an infinitesimally small volume dV , within a given homogeneously loaded structure with a total volume V_0 and the services stress σ , the probability of failure can be calculated like above. The term σ_0 represents the 63.2% of the LCF fatigue strength, measured during a standard fatigue specimen test with a given volume V_0 . The Weibull exponent m is a measure for the degree of natural scatter in fatigue experiments. A realistic range for m is [5,30]. A hypothetical material exhibiting virtually no scatter has $m \rightarrow \infty$.

The probability of survival Q_s in a given total volume V_0 , defined as $V_0 = MdV$ (where M is the number of volume elements), is reported in eq. A.2.

$$Q_s = 1 - P = \prod_{i=1}^M (1 - dP) = \left[1 - \left(\frac{\sigma}{\sigma_0}\right)^m \frac{1}{M}\right]^M \quad (\text{A.2})$$

For $M \rightarrow \infty$, A.2 can be written as

$$Q_s = \exp\left[-\left(\frac{\sigma}{\sigma_0}\right)^m\right] \quad (\text{A.3})$$

Since real parts usually have non-homogeneous stress levels in critical locations, eq.A.3 changes in eq.A.4.

$$Q_s = \exp\left[-\int_V \left(\frac{\sigma}{\sigma_0}\right)^m \frac{dV}{V_0}\right] \quad (\text{A.4})$$

To compare any random notched location to a standard LCF specimen, with a given surface area A_{smooth} and total Gauge section volume $V = V_{smooth}$, assuming

$Q_s = \text{constant}$, a failure equivalent notch stress level $\sigma_{notch,eq}$ have been defined (eq.A.5). This value corresponds to the allowable nominal stress level in a standard specimen, witch yield the same LCF life as the given notch part location.

$$\sigma_{notch,eq} = \left[\int_V (\sigma_{wp})^m \frac{dV}{V_{smooth}} \right]^{\frac{1}{m}} \quad (\text{A.5})$$

Usually, the weakest link theory is applied to volumes. For materials in witch critical defects occur mostly in the surfaces, or close to, the theory can be applied equivalently to an alternative definition for $\sigma_{notch,eq}$ (eq.A.6).

$$\sigma_{notch,eq} = \left[\int_A (\sigma_{wp})^m \frac{dA}{A_{smooth}} \right]^{\frac{1}{m}} = \sigma_{wl} \quad (\text{A.6})$$

This equation (A.6) gives the most accurate description for LCF in Nickel cast alloy [30].

Bibliography

- [1] J.Preuhs R. Schadt I. Wagner and P.R. Sahn. “New Aspects of Freckle Formation During Single Crystal Solidification of CMSX-4”. In: *Superalloys 2000* (2000), pp. 211–218. DOI: 10.7449/2000/superalloys_2000_211_218.
- [2] *MTU Aero Engines internal documentation*.
- [3] M. Yaguchi. “Anisotropic viscoplasticity constitutive model for directionally solidified superalloy”. In: *Materials at High Temperatures* 29.4 (2012), pp. 308–314. DOI: 10.3184/096034012X13485080639116.
- [4] R. C. Reed. *The Superalloys: Fundamentals and Applications*. Cambridge University Press, 2006. DOI: 10.1017/CB09780511541285.
- [5] S. Tin T. M. Pollock. “Nickel-based Superalloys for Advanced Turbine Engines: Chemistry, Microstructure, and Properties”. In: *Journal of Propulsion and Power* 22.22 (2006), pp. 361–374. DOI: 10.2514/1.18239.
- [6] W.C. Hagel C.T. Sims N.S. Stoloff. *Superalloys II*. Wiley-Interscience publication. Wiley, 1987. ISBN: 9780471011477. URL: <https://books.google.de/books?id=kqZTAAAAMAAJ>.
- [7] L. Kunz M. Smid S. Fintova and P. Hunter. “Role of defects in fatigue damage mechanisms of cast polycrystalline superalloy MAR-M 247”. In: *MATEC Web of Conferences* 12.03005 (2014), pp. 1–3. DOI: 10.1051/mateconf/20141203005.
- [8] L. Kunz M. Smid S. Fintova, P. Hunter, and K. Hrbacek. “Prediction of maximum casting defect size in MAR-M 247 alloy processed by hot isostatic pressing”. In: *Materials Engineering-Materialove inzinierstvo (MEMI)* 22.1 (2015), pp. 25–32. ISSN: 1338-6174.
- [9] H. Guo H. Tang. “Effect of grain defects on the mechanical behaviour of nickel-based single crystal superalloy”. In: *International Journal of Materials Research* 108.3 (2017), pp. 163–172. ISSN: 1862-5282. DOI: 10.3139/146.111466.
- [10] R. Metz H. Vehoff A. Nykyforchyn. “Fatigue crack nucleation at interfaces”. In: *Materials Science and Engineering:A* 387-389 (2004), pp. 546–551. ISSN: 0921-5093. DOI: <https://doi.org/10.1016/j.msea.2003.12.094>.
- [11] L Li et al. “Strain localization and fatigue cracking behaviors of Cu bicrystal with an inclined twin boundary”. In: *Acta Materialia* 73 (July 2014), pp. 167–176. DOI: 10.1016/j.actamat.2014.04.004.
- [12] M. Rupp. *MTU Aero Engines internal documentation, Einfluss von Querkorngrenzen auf die mechanischen von M-247LC SX*. Jan. 2014.

- [13] J. Belan. “Study of Advanced Materials for Aircraft Jet Engines Using Quantitative Metallography”. In: (2012). DOI: 10.5772/37254.
- [14] M. Gebura. “Chemical Composition and Classification of Single Crystal Nickel Base Superalloys”. In: *Materialovy inzinier 2007-2009* (2008), pp. 1–4.
- [15] L. Čelko I. Šulák K. Obrtlík. “Comparative Study of Microstructure and High Temperature Low Cycle Fatigue Behaviour of Nickel Base Superalloys Inconel 713LC and MAR-M247”. In: *Key Engineering Materials* 713 (Sept. 2016), p. 86. DOI: 10.4028/www.scientific.net/KEM.713.86.
- [16] A. M. S. Costa et al. “Creep Properties of Directionally Solidified Nb-Modified Ni-Base Superalloy, Mar-M247”. In: *Journal of Materials Engineering and Performance* 27.11 (Nov. 2018), pp. 5744–5751. ISSN: 1544-1024. DOI: 10.1007/s11665-018-3699-6. URL: <https://doi.org/10.1007/s11665-018-3699-6>.
- [17] M. Šmíd et al. “High Cycle Fatigue Damage Mechanisms of MAR-M 247 Superalloy at High Temperatures”. In: *Transactions of the Indian Institute of Metals* 69.2 (Mar. 2016), pp. 393–397. ISSN: 0975-1645. DOI: 10.1007/s12666-015-0817-0. URL: <https://doi.org/10.1007/s12666-015-0817-0>.
- [18] Gert Nolze. “Euler angles and crystal symmetry”. In: *Crystal Research and Technology* 50.2 (2015), pp. 188–201. DOI: 10.1002/crat.201400427. eprint: <https://onlinelibrary.wiley.com/doi/pdf/10.1002/crat.201400427>. URL: <https://onlinelibrary.wiley.com/doi/abs/10.1002/crat.201400427>.
- [19] Jianping Hong et al. “Freckle Defect Formation near the Casting Interfaces of Directionally Solidified Superalloys”. eng. In: *Materials* 9.11 (2016), p. 929. ISSN: 1996-1944.
- [20] D. Davidson et al. “4.05 - Small Fatigue Cracks”. In: *Comprehensive Structural Integrity*. Ed. by I. Milne, R.O. Ritchie, and B. Karihaloo. Oxford: Pergamon, 2003, pp. 129–164. ISBN: 978-0-08-043749-1. DOI: <https://doi.org/10.1016/B0-08-043749-4/04073-8>. URL: <http://www.sciencedirect.com/science/article/pii/B0080437494040738>.
- [21] P. Kazanowski. “Die Performance Optimization through Understanding of the Surface Features of Fatigue Fractures”. In: Hydro Aluminum Cedar Tools, May 2008.
- [22] B.K. Parida. “Fatigue Testing”. In: *Encyclopedia of Materials: Science and Technology*. Ed. by K.H. Jürgen Buschow et al. Oxford: Elsevier, 2001, pp. 2994–2999. ISBN: 978-0-08-043152-9. DOI: <https://doi.org/10.1016/B0-08-043152-6/00533-7>. URL: <http://www.sciencedirect.com/science/article/pii/B0080431526005337>.
- [23] Fabio Goedel, Gustavo P. Mezzomo, and Zacarias M. Chamberlain Pravia. “Fatigue lifespan of a fillet welded joint - Hybrid approach to obtain the S-N curve with a reduced number of tests”. en. In: *Latin American Journal of Solids and Structures* 15 (2018). ISSN: 1679-7825. URL: http://www.scielo.br/scielo.php?script=sci_arttext&pid=S1679-78252018001000509&nrm=iso.

-
- [24] Ueda Yukio, Murakawa Hidekazu, and Ma Ninshu. “The Finite Element Method”. In: *Welding Deformation and Residual Stress Prevention*. Elsevier, 2012, pp. 1–1. ISBN: 9780123948045.
- [25] *Altair Engineering Inc.* Sept. 2019. URL: <https://www.altair.de/>.
- [26] Sept. 2019. URL: <https://www.python.org/>.
- [27] *CalculiX.* Sept. 2019. URL: <http://www.calculix.de/>.
- [28] *Abaqus.* Sept. 2019. URL: <https://www.3ds.com/de/produkte-und-services/simulia/produkte/abacus/>.
- [29] Sept. 2019. URL: <https://de.wikipedia.org/wiki/Abaqus>.
- [30] M. Fried F. Vöse. *MTU Aero Engines internal documentation, Procedure to Assess Fatigue Life of M247LC-DS parts with grain defects: HABs/SNGs/TGBs.* July 2019.
- [31] *ABAQUS Analysis User’s Manual.* Sept. 2019. URL: <https://classes.engineering.wustl.edu/2009/spring/mase5513/abaqus/docs/v6.6/books/usb/default.htm?startat=pt05ch17s02abm02.html>.
- [32] Vitaliy Kindrachuk and Bernard Fedelich. “Simulation of Non-Isothermal Mechanical Tests on a Single Crystal Nickel-Basis Superalloy”. In: *Technische Mechanik* 32 (Jan. 2012), pp. 321–332.
- [33] Frank W. Zok. “On weakest link theory and Weibull statistics”. In: *Journal of the American Ceramic Society* 100.4 (2017), pp. 1265–1268. DOI: 10.1111/jace.14665. eprint: <https://ceramics.onlinelibrary.wiley.com/doi/pdf/10.1111/jace.14665>. URL: <https://ceramics.onlinelibrary.wiley.com/doi/abs/10.1111/jace.14665>.